SUPPORTING INFORMATION

Navigating *iR* Compensation: Practical Considerations for Accurate Study of Oxygen Evolution Catalytic Electrodes

Yoon Jun Son,[†] Raul A. Marquez,[‡] Kenta Kawashima,[‡] Lettie A. Smith,[‡]
Chikaodili E. Chukwuneke,[‡] Jerome Babauta,[§] C. Buddie Mullins*[,†,‡,††,‖,⊥]

[†] McKetta Department of Chemical Engineering, [‡] Department of Chemistry, [††] Texas Materials Institute, [‖]Center for Electrochemistry, and [⊥] H2@UT, The University of Texas at Austin, Austin, Texas 78712, United States. [§] Gamry Instruments, Warminster, Pennsylvania 18974, United States.

Corresponding author.

---

*E-mail: mullins@che.utexas.edu

Table of Contents

Experimental Methods

Materials and Chemicals. FTO glass (TEC 7, Sigma-Aldrich), Ni foil with a thickness of 0.05 mm and a purity of 99% (Thermo Scientific), and Ni foam with a thickness of 1.6 mm and a purity of 99.99% (MTI corporation) were used as substrates. Hydrochloric acid (Fisher Scientific), Ethanol (99.5%, PHARMCO), deionized (DI) water (> 18 MΩ cm resistivity), Potassium hydroxide (90%, flakes, Sigma-Aldrich), polydimethylsiloxane (PDMS) Sylgard 184 (Dow Corning), nickel nitrate hexahydrate with a purity of 99.9985% (Thermo Scientific), and cobalt nitrate hexahydrate with a purity of 99.9% (Thermo Scientific) were used without further purification.

Electrode Preparation. FTO glass was ultrasonically cleaned using ethanol and DI water for 10 min each and dried with compressed air. The surface of the FTO glass was masked using a 3M 470 electroplating tape and a geometric area of ~0.5 cm^2 of FTO was left exposed. Ni foil was first ultrasonically cleaned using ethanol and DI water for 10 min each. Then, Ni foil was electropolished in 15 mL of a 50 wt% H_2SO_4 bath at 500 mA for 60 s (30 s per each side) using a Ni foam with a size of 5 cm^2 as a counter electrode. After electropolishing, Ni foil was rinsed with DI water and dried at room temperature. After drying, a PDMS coating was applied to expose only an active area of ~1 cm^2. PDMS was prepared as a mixture of the base and curing agent in an 8:1 ratio, respectively, and then mixed thoroughly for 10 min. The PDMS-coated Ni foil was dried at 40ºC for 2 h in an oven. A solution for electrodeposition was prepared by dissolving 20 mM transition metal nitrate in DI water and stirring the solution for 2 h at 25 °C. For example, 20 mM $Ni(NO_3)_2$ for $Ni(OH)_2$ electrodeposition, 20 mM $Co(NO_3)_2$ for $Co(OH)_2$ electrodeposition, 10 mM $Ni(NO_3)_2$ and 10 mM $Co(NO_3)_2$ for $NiCo(OH)_2$ electrodeposition were used. Also, the pH of the electrodeposition solution was adjusted to ~3 with 1 M HNO_3. For electrodeposition of $Ni(OH)_2$, $Co(OH)_2$, and $NiCo(OH)_2$ film on FTO glass substrate and $Ni(OH)_2$ film on Ni foil substrate, galvanostatic electrodeposition was conducted at 1 mA/cm^2 with a two-electrode configuration employing graphite or Ni foam as counter electrodes. The electrodeposition time for metal hydroxides on the FTO substrate was 15 or 30 s and that on Ni foil was 300 s. After electrodeposition, electrodes were carefully rinsed with DI water, dried with compressed air, and stored under ambient conditions. The nanoporous NiO_xH_y/Ni foam sample was prepared according to the previous method using electrochemical anodization.[1]

Electrochemical Measurements. Electrochemical analyses for all experimental samples were carried out in Fe-purified 1 M KOH electrolyte except for the nanoporous NiO_xH_y/Ni foam sample in Fe-unpurified 1 M KOH electrolyte. An Fe-unpurified 1 M KOH electrolyte was prepared by dissolving KOH solid salts in pure DI water. An Fe-purified 1 M KOH electrolyte was prepared by purifying a Fe-unpurified 1 M KOH electrolyte according to the previous method using the absorption of Fe by $Ni(OH)_2$.[2,3] A polypropylene container was washed with 0.5 M H_2SO_4 and DI water to remove any remaining impurities, and then was employed as an electrochemical reactor for electrodeposition or electrochemical analyses to avoid any possible contamination (*e.g.*, glass-etching in alkaline media). Polytetrafluoroethylene (PTFE)-based electrode holders with either titanium (Ti) or platinum (Pt) sheet or stainless alligator clip were used to connect the working electrode to a potentiostat. Electrochemical analyses were conducted using a Reference 620 potentiostat/galvanostat (Gamry Instrument, USA) with a three-electrode configuration. A graphite rod and Hg/HgO in 1 M KOH served as counter and reference electrodes, respectively. All the potentials (E) applied for electrochemical analyses were converted into reversible hydrogen electrode (V *vs.* RHE) scale according to the Nernst equation [$E = E_{\mathrm{Hg/HgO}} + 0.059 \times \mathrm{pH} + E°_{\mathrm{Hg/HgO}}$], where $E_{\mathrm{Hg/HgO}}$ is the applied potential *vs.* Hg/HgO reference electrode and $E°_{\mathrm{Hg/HgO}}$ in 1 M KOH at 25 °C is 0.098 V. Electrochemical impedance spectroscopy (EIS) analyses were conducted at several different potentials in the frequency range from 5×10^{-2} to 10^6 Hz with 10 mV of amplitude. CV analyses were conducted in the potential range of 1.10–1.68 V at a scan rate of 10 mV/s. For R_u measurement, three different methods were employed including (1) automatic EIS-based R_u measurement using the potentiostat software (*e.g.*, Gamry Framework), (2) manual EIS, and (3) current interrupt. Concerning the reproducibility of R_u data, when using fresh samples of the same electrode, there were slight variations in the measured R_u values, typically within around 1 Ω cm^2, which is attributed to experimental variations. However, it is important to note that the general trend of distinct R_u values obtained through different R_u measurement methods (*e.g.*, $R_{u,\mathrm{CI}}$ and $R_{u,\mathrm{EIS}}$) reported in this Viewpoint was consistent and reproducible across multiple samples and during repetitive electrochemical tests. Also, different types of *iR* compensation techniques including positive feedback (PF), current interrupt (CI), and post-*iR* *(*Post*)* compensation were employed for CV analyses. Scan rate-dependent CV analyses for NiO_xH_y/FTO, CoO_xH_y/FTO, and $NiCoO_xH_y$/FTO samples were conducted at scan rates of 2, 4, 6, 8, 10, 20, 40, 60, 80, and 100 mV/s. Gamry Echem Analyst was used to analyze the R_u from the plot of V_u *versus* j and the actual scan rate from the plot of applied potential *versus* time during the CV. To prepare the Ni-CV sample, CV electrochemical conditioning was conducted for Ni foil at a scan rate of 20 mV/s in the potential range of 1.10–1.68 V for 1000 cycles without *iR* compensation.

Supporting Note 1. R_u measurement and *iR* compensation methods

There are two commonly used methods to measure R_u: AC technique-based EIS (either manual or automatic) and DC technique-based current interruption. In EIS, an AC signal is applied to the electrochemical system across a range of frequencies. By analyzing the impedance response of the electrochemical system, R_u can be determined within the high-frequency region. In manual EIS, the obtained EIS data are fitted manually, and R_u is identified as the series resistance. Automatic EIS, also known as automatic R_u measurement, is carried out using software and measures R_u at the point where the phase shift approaches zero (*i.e.*, lowest imaginary impedance) or the first inflection point in the high-frequency region. On the other hand, current interruption involves intermittently interrupting the current flow in the electrochemical system while setting the potential of the working electrode to the open circuit potential. By measuring the voltage drop during these interruptions, the current interruption method assesses the *iR* potential drop caused by the series resistance (or R_u) in the electrochemical system (see **Supporting Note 2.6** and **Figure S19a** for details about R_u measurement by current interruption).

Different methods (*e.g.*, PF, CI, and Post) and degrees (*e.g.*, full 100% and partial 85%) of *iR* compensation can be employed, such as CI, PF 100%, PF 85%, Post 100%, and PF 85% + Post 15%. These *iR* compensation methods offer various characteristics and considerations. In terms of the R_u value used for each *iR* compensation method, the CI method utilizes the R_u values measured during the electrochemical analysis through current interruption. This allows the CI method to account for the *in situ* variation of R_u with applied potential and operating current during the electrochemical analysis. In contrast, the PF and Post methods rely on the R_u measured by EIS prior to *iR* compensation. These methods assume that the R_u value remains constant throughout the electrochemical analysis, although this may not always be the case. Regarding the degree of *iR* compensation, the CI method compensates for 100% of the measured R_u. On the other hand, the PF method commonly employs a partial degree of compensation that is less than 100%. This is due to the poor stability of the potentiostat when attempting to achieve 100% PF compensation, which can result in oscillations of the *iR*-compensated electrochemical signal. For the Post method, a 100% degree of *iR* compensation is commonly applied.

In addition to the characteristics mentioned earlier, there are further considerations for the *iR* compensation methods. The CI method requires a sufficiently large faradaic capacitance as well as faradaic resistance larger than R_u for accurate measurement. Additionally, the CI method is not suitable for situations where fast measurements are required, such as when using a scan rate greater than 100 mV/s. On the other hand, the PF method is more appropriate for fast electrochemical experiments such as cyclic voltammetry even with fast scan rates. Also, note that the Post method has a limitation regarding potential window changes after *iR* compensation. This means that the complete potential window cannot be determined until the post-*iR* compensation is completed. Consequently, the Post method is not proper for studying redox peak properties as it can result in the distortion of information such as redox peak potential, the peak-to-peak separation between anodic and cathodic redox peak potentials, and redox peak current.

Table S1. Summary of prepared electrodes sorted according to the characteristics (*i.e.*, type, composition, morphology, thickness, and electrical conductivity) of catalyst layer, substrate, and electrode holder.

Sample	**Catalyst layer**				**Substrate**			**Electrode holder**
	Composition	Morphology/ Thickness	Electrical conductivity		Type	Morphology/ Thickness	Electrical conductivity	Type
			Initial	Switching during redox				
NiO_xH_y/FTO	NiO_xH_y	Compact/ Thin	Low	Yes	FTO glass	2D/ Thick	Low	Alligator clip Ti holder Pt holder
CoO_xH_y/FTO	CoO_xH_y	Compact/ Thin	High	Negligible				
$NiCoO_xH_y$/FTO	$NiCoO_xH_y$	Compact/ Thin	Medium	Yes				
Ni foil	NiO_xH_y	Compact/ Very Thin	High	Negligible	Ni foil	2D/ Thin	High	
Ni foil-CV	NiO_xH_y	Compact/ Thick	Low	Yes				
NiO_xH_y/Ni foil	NiO_xH_y	Compact/ Thick	Low	Yes				
Peeled-off NiO_xH_y/Ni foil	NiO_xH_y	Compact/ Very Thin	High	Negligible				
Nanoporous NiO_xH_y /Ni foam	Fe-doped NiO_xH_y	Porous/ Thick	Low	Yes	Ni foam	3D/ Compressible (~Thin)	High	

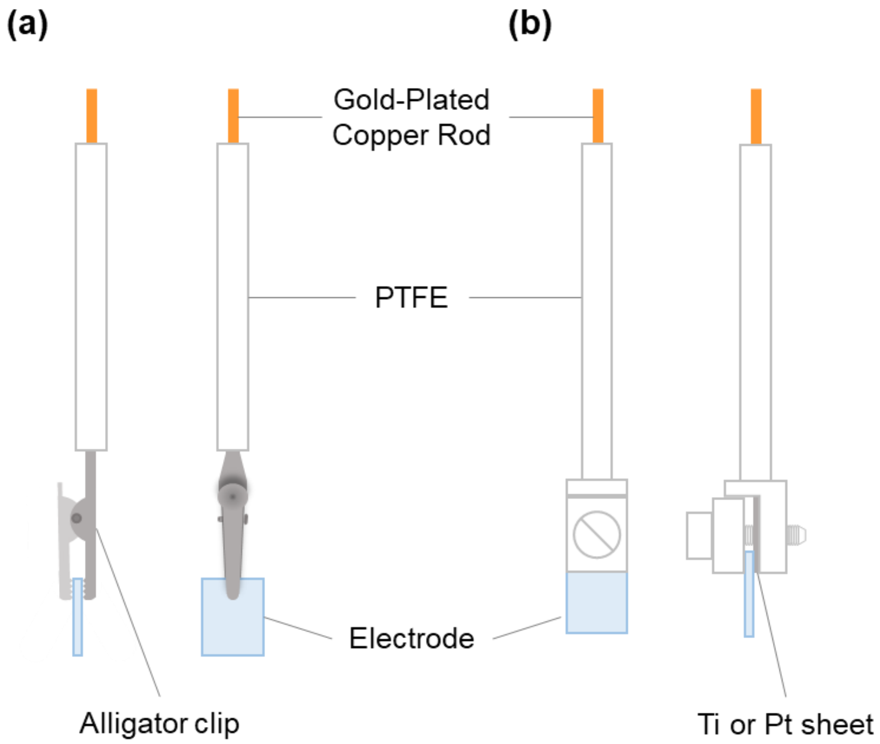

Figure S1. Schematic illustrations of different types of polytetrafluoroethylene (PTFE)-based electrode holders: (a) alligator (stainless or aluminum) clip and (b) titanium (Ti) or platinum (Pt) clip. Here, Ti wire inside the PTFE electrically connects the gold-plated copper rod with an alligator clip and Ti or Pt sheet.

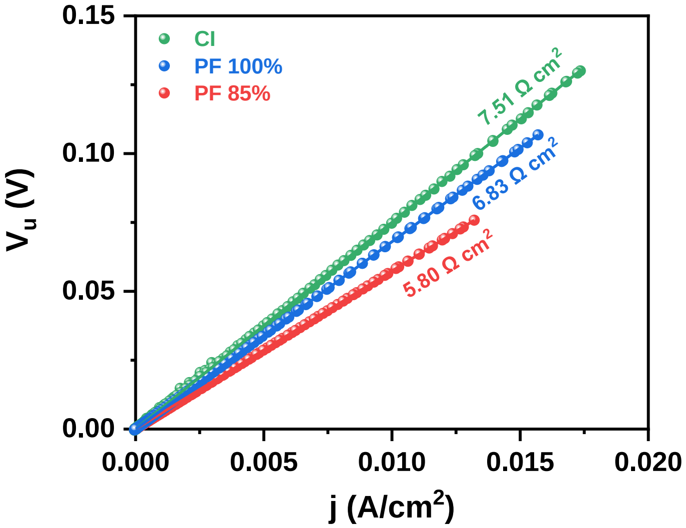

Figure S2. Plots of uncompensated potential (V_u) *versus* current density (j) for the NiO_xH_y/FTO electrode in **Figure 2a**. The R_u values used during the CV analyses can be estimated from the slope of plot of V_u vs. j.

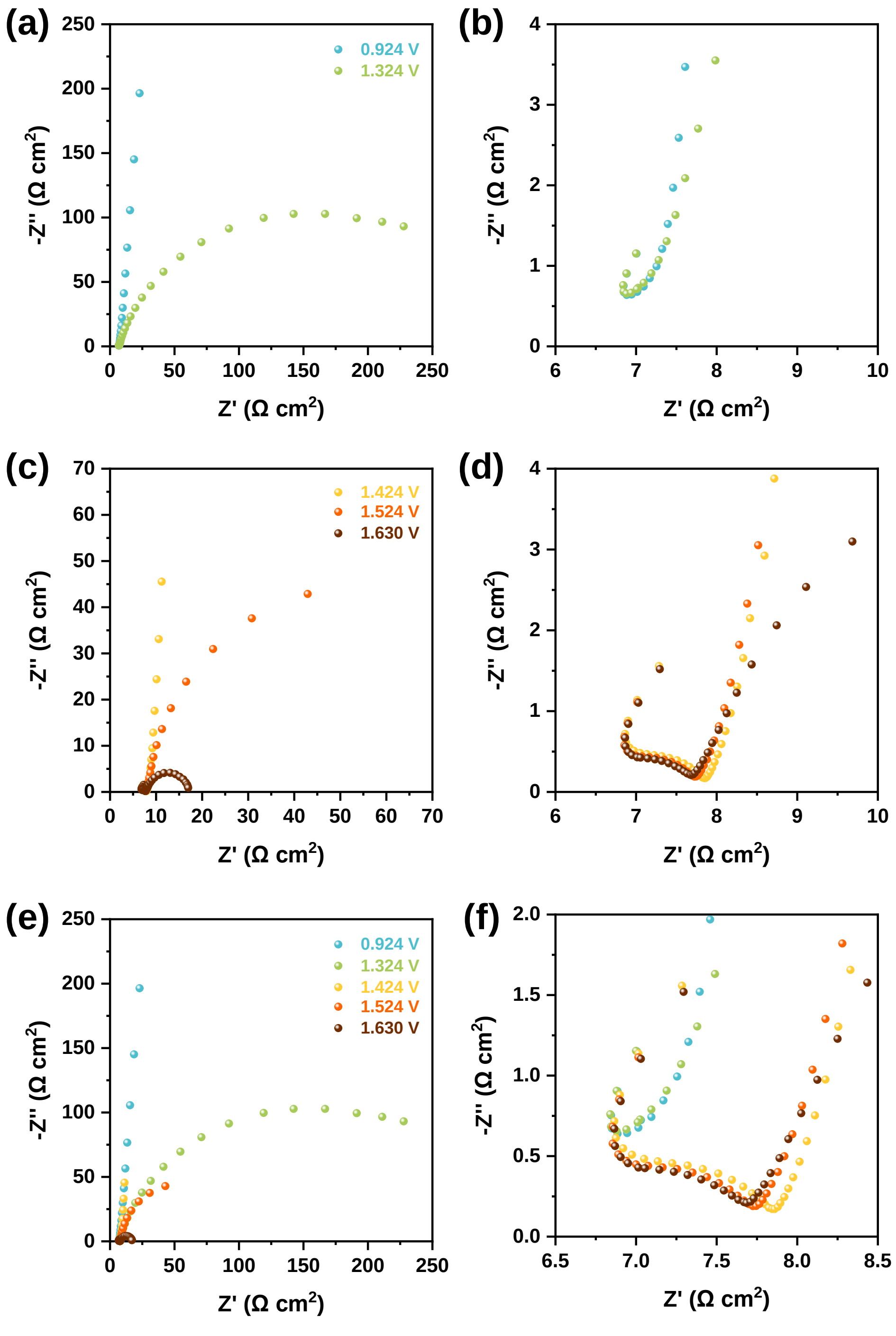

Figure S3. EIS Nyquist plots of the NiO_xH_y/FTO electrode in **Figure 2a** at different potentials (V *vs.* RHE) (a,b) below and (c,d) above the potential for anodic $Ni^{2+/3+}$ redox reaction, and (e,f) overlap of **Figure S2a,b**.

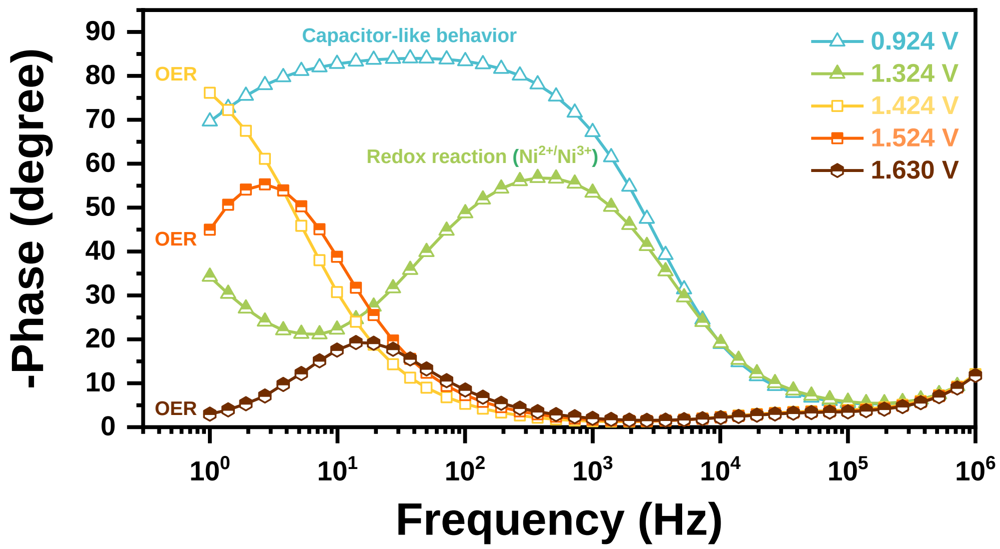

Figure S4. EIS Bode phase plots of the NiO_xH_y/FTO electrode in **Figure 2a** at different potentials.

Supporting Note 2. Contact impedance

2.1. Identification of contact impedance at the electrode holder/substrate interface

Figure S3 shows the EIS Nyquist plots of the NiO_xH_y/FTO electrode at various potentials, both before and after the $Ni^{2+/3+}$ anodic redox reaction. In **Figure S3a,b**, the EIS Nyquist plots obtained at 0.924 V and 1.324 V, which are lower than the anodic redox peak potential for $Ni^{2+/3+}$ at approximately 1.36 V demonstrate two distinct behaviors. The plot at 0.924 V displays a vertical increase, indicating capacitive behavior, while the plot at 1.324 V shows a single semicircle representing the $Ni^{2+/3+}$ anodic redox reaction. On the other hand, in **Figure S3c,d**, EIS Nyquist plots obtained at 1.424 V, 1.524 V, and 1.630 V, which exceed 1.36 V, exhibit two semicircles.

The Bode phase plots in **Figure S4** can help to identify the potential-dependent impedance signal by providing the frequency distribution of the obtained EIS data. The Bode phase plot at 0.924 V exhibits a plateau with a 90-degree phase shift, indicating capacitor-like behavior. At 1.324 V, the Bode phase plot shows a peak at the frequency of 10^2–10^4 Hz, which is indicative of faradaic impedance for the $Ni^{2+/3+}$ anodic redox reaction. On the other hand, the Bode phase plots at 1.424 V, 1.524 V, and 1.630 V display peaks at lower frequency regions compared to the $Ni^{2+/3+}$ anodic redox reaction. The peak at 1.630 V represents the faradaic impedance for the OER as it is the only faradaic reaction observed at that potential. Additionally, the peak corresponding to OER impedance gradually shifts to higher frequency regions with increasing potential from 1.424 to 1.630 V vs RHE. This increase is expected as increasing potential would provide a greater driving force for the OER reaction to occur. Furthermore, the peak at the higher frequency region at 1.324 V can be distinguished from the OER impedance peaks at lower frequency regions at potentials equal to or greater than 1.424 V due to the faster kinetics of the $Ni^{2+/3+}$ redox reaction compared to the sluggish OER. In **Figure S4**, slight phase shifts in the high-frequency region from 10−100 kHz were also observed at 1.424 V, 1.524 V, and 1.630 V, corresponding to the appearance of an additional semicircle in the high-frequency region of the Nyquist plots in **Figure S3c,d**. This high-frequency impedance is not discernible at potentials below the anodic redox potential for $Ni^{2+/3+}$ (*e.g.*, 0.924 and 1.324 V) due to its overlap with capacitor-like behavior (at 0.924 V) or the impedance response for $Ni^{2+/3+}$ redox reaction (at 1.324 V) with relatively fast kinetics in the high-frequency range. However, at potentials above the anodic redox potential for $Ni^{2+/3+}$ (*e.g.*, 1.424 V, 1.524 V, and 1.630 V), which correspond to OER potentials, this high-frequency impedance becomes noticeable. This emergence of a high-frequency impedance feature at potentials relevant to the OER is not the result of reaching larger anodic potentials, rather, it only becomes discernable at these potentials because the OER impedance response does not overlap with the high-frequency impedance due to the lower kinetics and lower frequency range associated with the OER.

To gain further insight into the nature of the high-frequency impedance observed at 10^4−10^5 Hz, additional control experiments were conducted. First, EIS analyses were conducted at various potentials for a pure FTO substrate to exclude any interference of catalyst layer (**Figure S5)**. For the FTO substrate, the high-frequency impedance was not observed across all potentials examined. However, it is challenging to determine the presence or absence of the high-frequency impedance based solely on this outcome. The reason behind this uncertainty lies in the fact that the only faradaic reaction, which is the oxidation/dissolution reaction of FTO occurring above 1.524 V, exhibits rapid kinetics and takes place within the high-frequency range that overlaps with the 10^4−10^5 Hz range of the high-frequency impedance. Based on the findings, the high-frequency impedance is not caused by FTO oxidation/dissolution (**Figure S5**) or $Ni^{2+/3+}$ redox reaction, or the OER (**Figure S3** and **S4**). Hence, it can be concluded that the high-frequency impedance is unrelated to the faradaic reactions within the electrochemical system. Instead, it likely originates from some other phenomenon occurring at the working electrode.

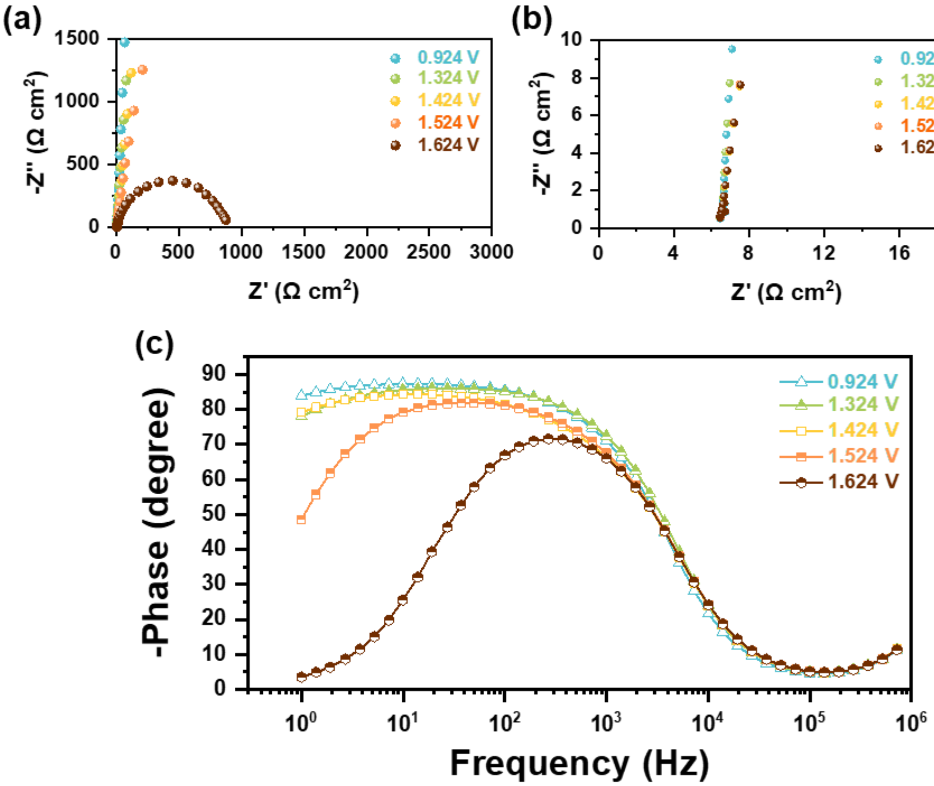

Figure S5. EIS spectra of FTO substrate at different potentials. (a,b) Nyquist plots and (c) Bode phase plots.

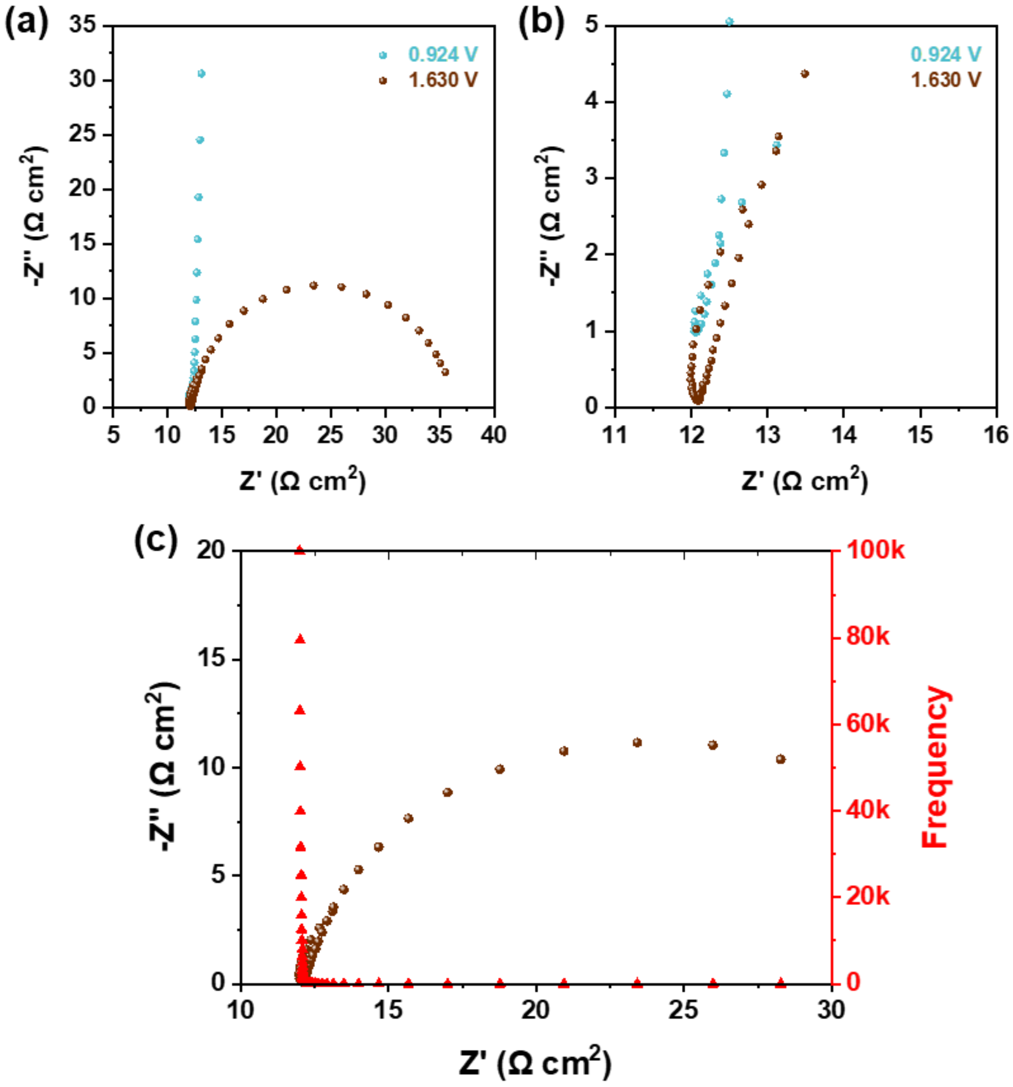

Figure S6. EIS spectra of the NiO_xH_y/FTO electrode connected with a Pt electrode holder. (a,b) Nyquist plots at 0.924 and 1.63 V, and (c) Nyquist plot at 1.630 V with the corresponding frequency.

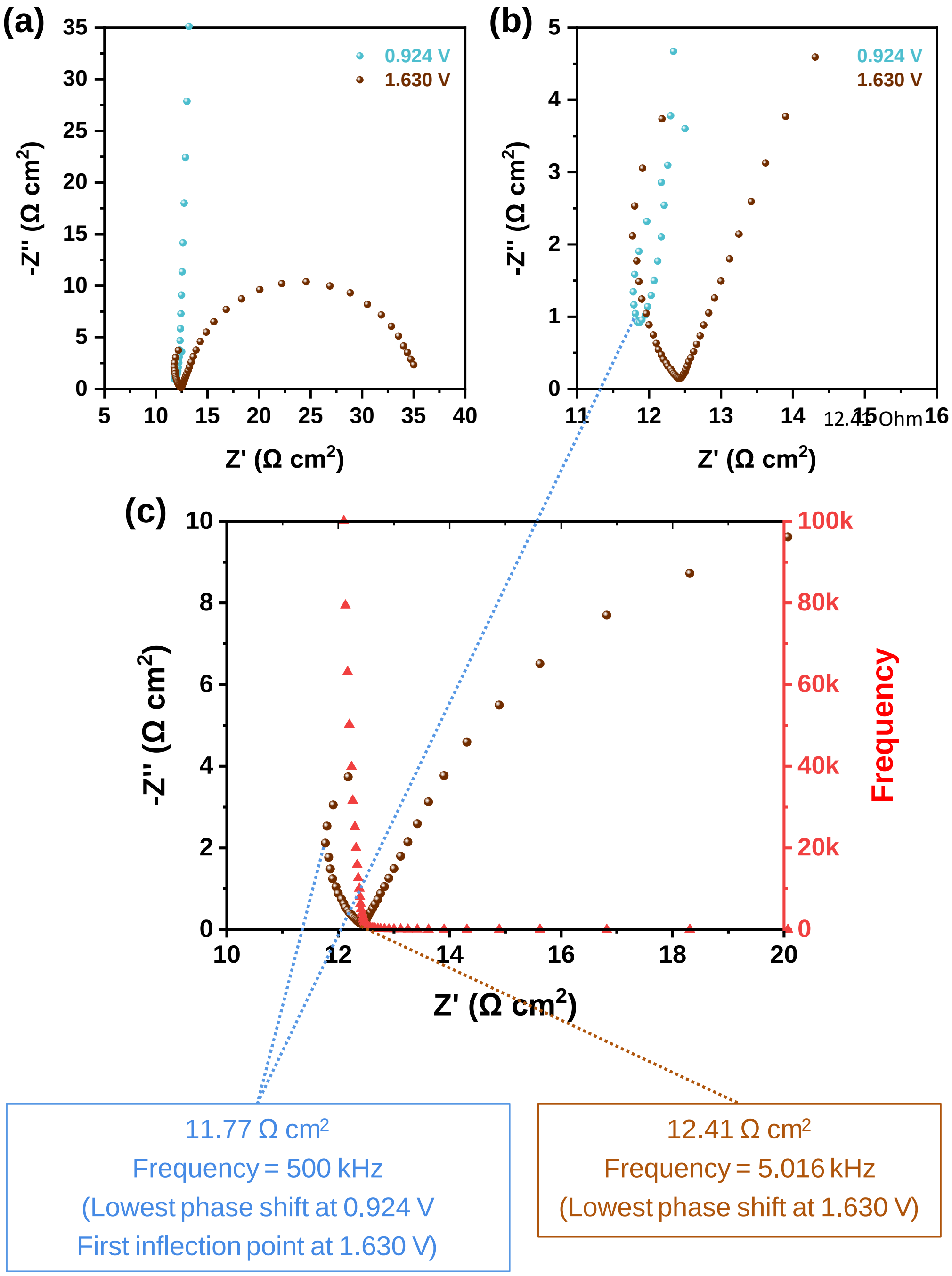

11.77 Ω cm^2
Frequency = 500 kHz
(Lowest phase shift at 0.924 V
First inflection point at 1.630 V)

12.41 Ω cm^2
Frequency = 5.016 kHz
(Lowest phase shift at 1.630 V)

Figure S7. EIS spectra of the NiO_xH_y/FTO electrode connected with a Ti electrode holder. (a,b) Nyquist plots at 0.924 and 1.63 V, and (c) Nyquist plot at 1.630 V with the corresponding frequency.

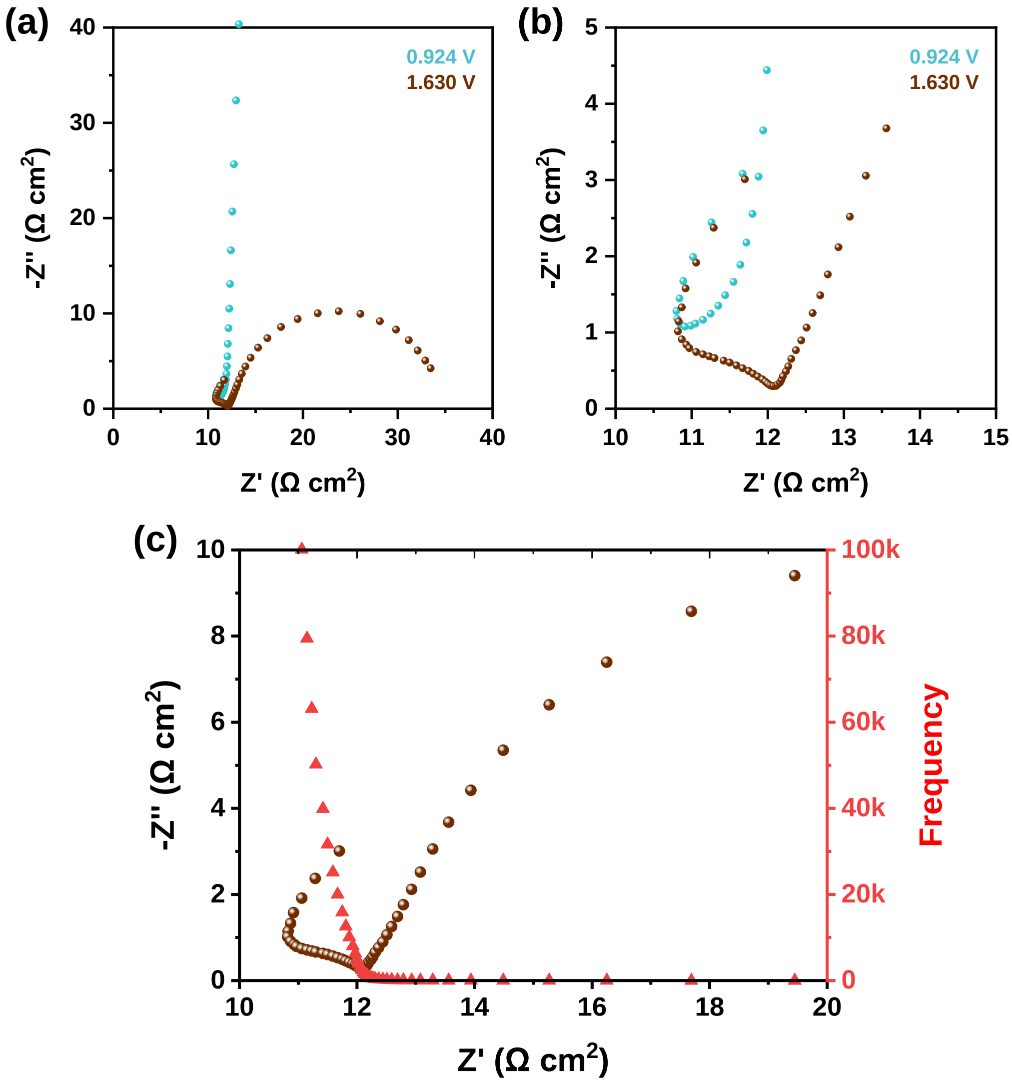

Figure S8. EIS spectra of the NiO$_x$H$_y$/FTO electrode connected with an alligator clip. (a,b) Nyquist plots at 0.924 and 1.63 V, and (c) Nyquist plot at 1.630 V with the corresponding frequency.

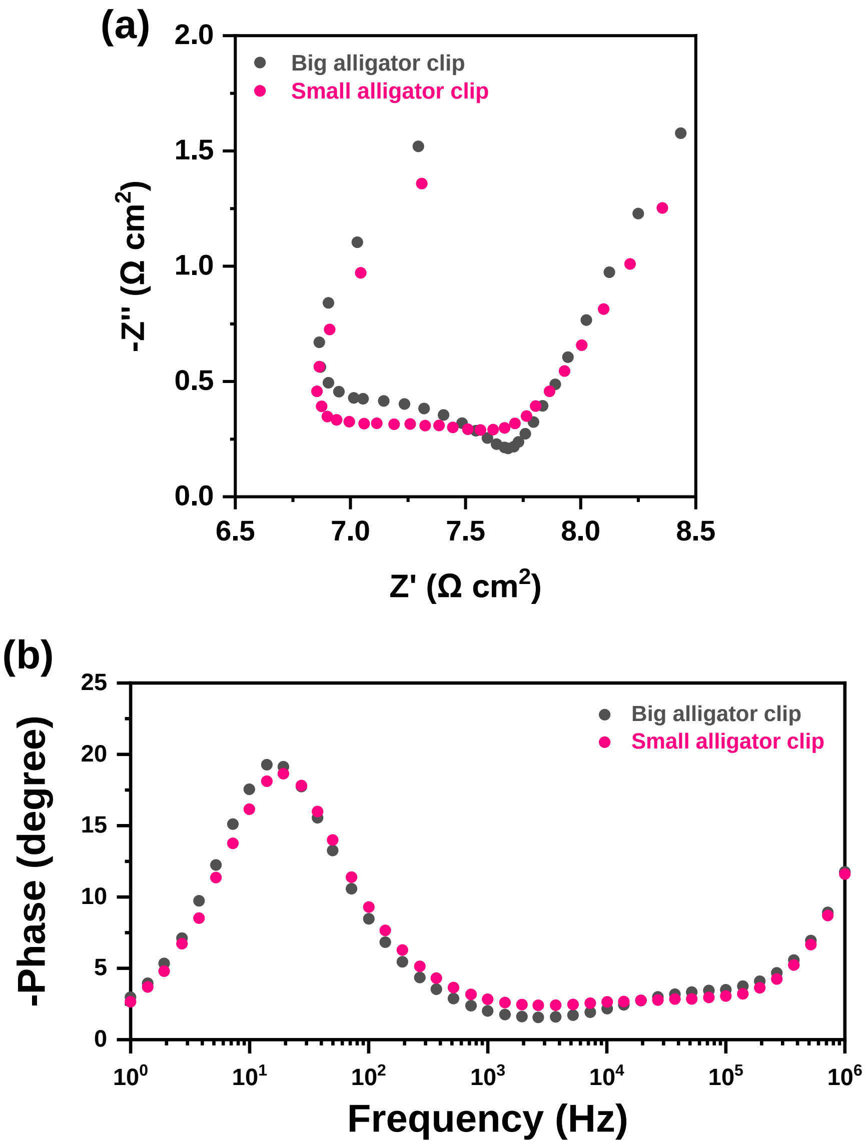

Figure S9. EIS spectra of the NiO_xH_y/FTO electrode in **Figure 2a** at 1.630 V connected with big and small alligator clips. (a) Nyquist plots and (b) Bode phase plots.

The control experiments conducted using different types of electrode holders (**Figure S6-S9**) provide valuable insights into the nature of the high-frequency impedance. The results demonstrate that the high-frequency impedance is a contact impedance that arises at the interface between the electrode holder and the substrate. When a Pt clip is used as the electrode holder, the EIS Nyquist plot at 1.630 V displays only a single semicircle (**Figure S6**). Additionally, the EIS data points in the high-frequency region (1−100 kHz) exhibit nearly identical real impedance values without dispersion, and the evaluated R_u values were consistent across different applied potentials. These characteristics indicate the absence of high-frequency impedance when employing a Pt clip as the electrode holder. When a Ti clip is used as the electrode holder, only a single semicircle was observed at 1.630 V (**Figure S7**). However, unlike the case with the Pt clip, the EIS data points in the high-frequency region (above 5 kHz) were dispersed, and distinct R_u values were obtained depending on the applied potential. These findings suggest the presence of high-frequency impedance with a small contribution from capacitance. When an alligator clip (not polished) is employed as the electrode holder, two semicircles were observed at 1.630 V due to the occurrence of an additional semicircle in the high-frequency region (**Figure S8)**. Furthermore, the EIS data points in the high-frequency region (above 5 kHz) showed even greater dispersion compared to the case with a Ti clip, and distinct R_u values were obtained depending on the applied potential. These characteristics confirm the presence of high-frequency impedance arising from the contact between the electrode and electrode holder. Moreover, in **Figure S9**, when a smaller alligator clip is utilized, the phase shift associated with the high-frequency impedance becomes less significant due to the smaller contact area and lower capacitance of the electrode holder. Overall, these control experiments with different electrode holders provide evidence that the high-frequency impedance observed is primarily caused by the contact impedance at the electrode holder/substrate interface.

2.2. Origin of contact impedance at electrode holder/substrate interface and how to avoid it

The phase shift observed in EIS analysis, particularly in the form of a peak on the Bode phase plot, indicates that the contact impedance at the electrode holder/substrate interface consists of capacitance and resistance in parallel. The capacitance at the contact can be generated when an oxide layer forms on the surface of either the electrode holder or the substrate, resulting in a conductor (*e.g.*, electrode holder)/insulator (*e.g.*, surface oxide layer)/conductor (*e.g.*, substrate) interface. Note that in the case where there is no surface oxide formation and only a conductor/conductor interface exists, there is no capacitance present, and only contact resistance exists due to the junction potential between two different types of conductors. The presence and characteristics of the contact impedance at the electrode holder/substrate interface are influenced by various factors, including the type of electrode holder and substrate, and the specific experimental conditions.

The material properties of the electrode holder and substrate play a crucial role in determining the presence and characteristics of contact impedance formation. One important factor is the resistance to surface oxidation, which affects the potential for contact impedance to occur. For instance, an alligator clip, commonly made of materials such as stainless steel, nickel-plated steel, or copper, is prone to surface oxidation even under ambient conditions, resulting in the formation of a thin oxide layer. Similarly, the titanium metal present in the Ti clip is also susceptible to surface oxidation. Therefore, both the alligator clip and Ti clip have the potential to induce contact impedance. In contrast, a Pt clip is less likely to cause contact impedance due to the strong resistance of platinum to surface oxidation. When it comes to the substrate, transition metal-based substrates like Ni foil and Ni foam can also form a surface oxide layer under ambient conditions, making them susceptible to contact impedance formation. In addition to resistance to surface oxidation, the electrical conductivity and thickness of the oxide layer can also influence the magnitude of the contact impedance.

The experimental conditions also play a significant role in determining the presence and magnitude of contact impedance. During OER testing, the electrode holder is often exposed to alkaline electrolytes in various ways. This exposure can occur through the immersion of the electrode holder into the electrolyte together with the catalytic electrode,[4] wetting of the electrode holder by the electrolyte due to the capillary effect through foam-type electrodes like Ni foam,[4] or even evaporation of the electrolyte during electrochemical testing, as observed through experience. When alligator clips and Ti clips are exposed to alkaline electrolyte, their surface oxidation is facilitated, making contact impedance formation more likely at the electrode holder/substrate interface. Consequently, the development of contact impedance during long-term electrochemical testing is sometimes inevitable. However, it is worth noting that even though Pt clips are less prone to forming contact impedance, they have a critical limitation. When exposed to alkaline electrolytes under positive potential, Pt can still undergo oxidation and form Pt oxide. This Pt oxide is easily dissolved into the electrolyte. The dissolved Pt can then be deposited onto the working electrode, leading to an erroneous evaluation of catalytic performance. This dissolution is also why the use of Pt counter electrodes is avoided when studying non-noble metal-based electrocatalysts. Therefore, the experimental conditions, particularly the exposure to alkaline electrolytes, can significantly impact the formation of contact impedance, and each type of electrode holder has its own limitations regarding oxidation and potential interference with the electrochemical system.

To avoid the contact impedance at the electrode holder/substrate interface, the surface oxide layer must be eliminated. This can be achieved through various methods such as sanding the surface of the electrode holder with sandpaper, or using sonication or electropolishing techniques on the electrode holder and substrate in an acidic solution (*e.g.*, 1 M HCl). It is advisable to use a clean electrode holder and substrate for electrochemical testing immediately after removing the surface oxide layer, before the surface oxide layer reforms under ambient conditions. Moreover, to confirm the absence of the surface oxide layer and any resulting contact impedance, it is recommended to perform potential-dependent EIS analysis at potentials both within and beyond the range of the slow faradaic reaction (*e.g.*, OER). This allows for a clear assessment of the presence or absence of contact impedance.

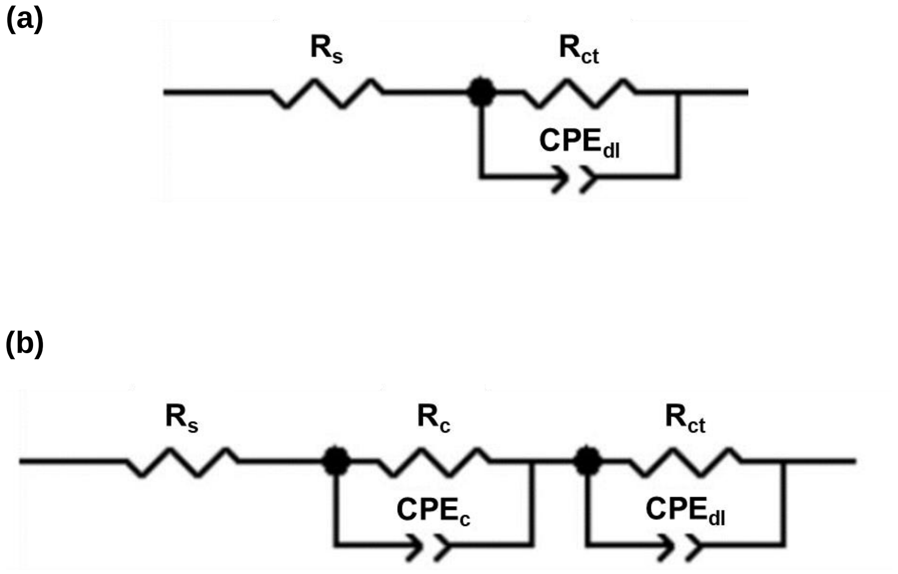

Figure S10. Equivalent circuit models for catalytic electrodes (a) without contact impedance and (b) with contact impedance.

2.3. Equivalent circuit models with and without contact impedance

Figure S10 shows the equivalent circuit models for catalytic electrode (a) without contact impedance and (b) with contact impedance. In **Figure S10b**, the catalytic electrode with the contact impedance includes an additional RC circuit representing the contact impedance, in addition to the RC circuit associated with the faradaic reaction (*e.g.*, OER) shown in **Figure S10a**. Here, R_s is a series resistance. R_{ct} is a charge transfer resistance at the catalyst/electrolyte interface and CPE_{ct} is a constant phase element reflecting the catalytic interface. R_c and CPE_c in parallel represent the contact impedance. Capacitance (C) was calculated according to the following equation, $C = CPE \times (w_{max})^{n-1}$, where w_{max} is the frequency at which the imaginary component reaches a maximum and n represents the ideality of capacitance and has a value between 0 and 1. Additionally, it is noted that the RC time constant, which is the reciprocal of the frequency in EIS data, for the contact impedance is smaller compared to the faradaic impedance. This is due to smaller contact capacitance compared to the faradaic capacitance at the catalyst/electrolyte interface (*i.e.*, electrochemical double-layer capacitance). As a result, contact impedance is observed in the higher frequency range compared to the faradaic impedance.

2.4. Different shapes of contact impedance

The contact impedance, which is composed of capacitance and resistance in parallel, exhibits different shapes depending on its characteristics, specifically the ratio of capacitance to resistance. In this study, the contact impedance was categorized into three types based on its shape;

Type 1 contact impedance is characterized by a relatively flat shape on the Nyquist plot, lacking a clear semicircle shape. The phase shift observed on the Bode phase plot is negligible.

Type 2 contact impedance exhibits a small or ambiguous semicircle shape on the Nyquist plot, accompanied by a relatively small phase shift on the Bode phase plot.

Type 3 contact impedance displays a clear semicircle shape on the Nyquist plot, accompanied by a distinct phase shift on the Bode phase plot.

Electrochemical analysis results of the NiO_xH_y/FTO electrode with different types of contact impedance are shown in **Figures S2, S3**, and **S11-S18**: **Figures S2**, **S3**, **S11**, and **S12** for Type 2, **Figures S13-S15** for Type 1, and **Figures S16-S18** for Type 3 contact impedance. These figures include Nyquist plots with descriptions about $R_{\mathrm{u,EIS,1}}$, $R_{\mathrm{u,CI}}$, and $R_{\mathrm{u,EIS,2}}$ values, as well as Bode phase plots and CV curves using different R_{u} values for *iR* compensation. Additionally, note that fitting the EIS data using an equivalent circuit in **Figure S10b** is viable for the Type 3 contact impedance, characterized by a clearly discernible semicircle on the Nyquist plot. However, EIS fitting becomes challenging for Type 1 and Type 2 contact impedance, where there is a small phase shift or overlap between contact impedance and the roll-off effects caused by instrumentation, making the semicircle shape not well-defined in the Nyquist plot. In such cases, the recommended approach for estimating contact resistance within the contact impedance is to compare the difference between $R_{\mathrm{u,EIS,2}}$ and $R_{\mathrm{u,EIS,1}}$. Here, $R_{\mathrm{u,EIS,1}}$ can be determined either at the first inflection point or the point of the lowest phase angle in the high-frequency region from EIS at non-faradaic potentials, or at the first inflection point from EIS at faradaic potentials. On the other hand, $R_{\mathrm{u,EIS,2}}$ can be measured at the lowest phase angle point from EIS at faradaic potentials.

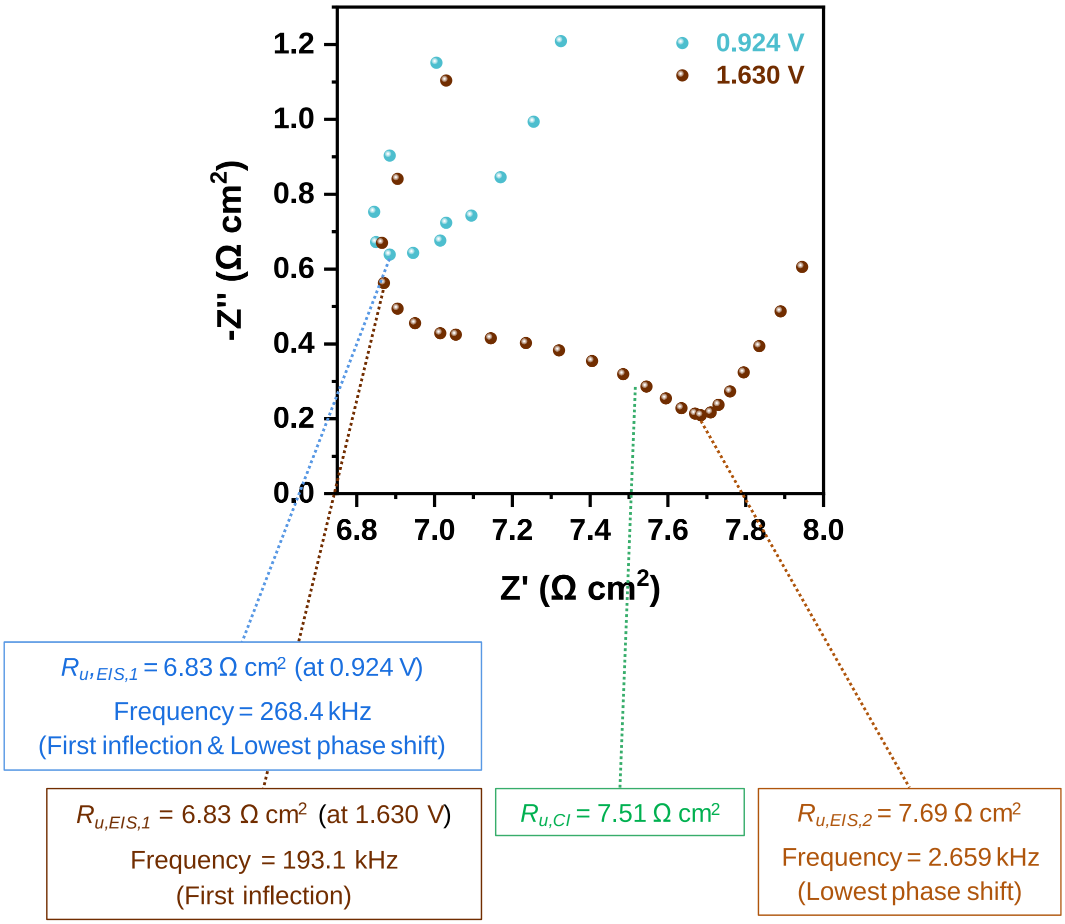

$R_{u,EIS,1}$ = 6.83 Ω cm^2 (at 0.924 V)
Frequency = 268.4 kHz
(First inflection & Lowest phase shift)

$R_{u,EIS,1}$ = 6.83 Ω cm^2 (at 1.630 V)
Frequency = 193.1 kHz
(First inflection)

$R_{u,CI}$ = 7.51 Ω cm^2

$R_{u,EIS,2}$ = 7.69 Ω cm^2
Frequency = 2.659 kHz
(Lowest phase shift)

Figure S11. Comparison of possible R_u value options (*i.e.*, $R_{u,EIS,1}$, $R_{u,CI}$, and $R_{u,EIS,2}$) for *iR* compensation based on EIS Nyquist plots of the NiO_xH_y/FTO electrode with Type 2 contact impedance in **Figure 2a** and **Figure S2.**

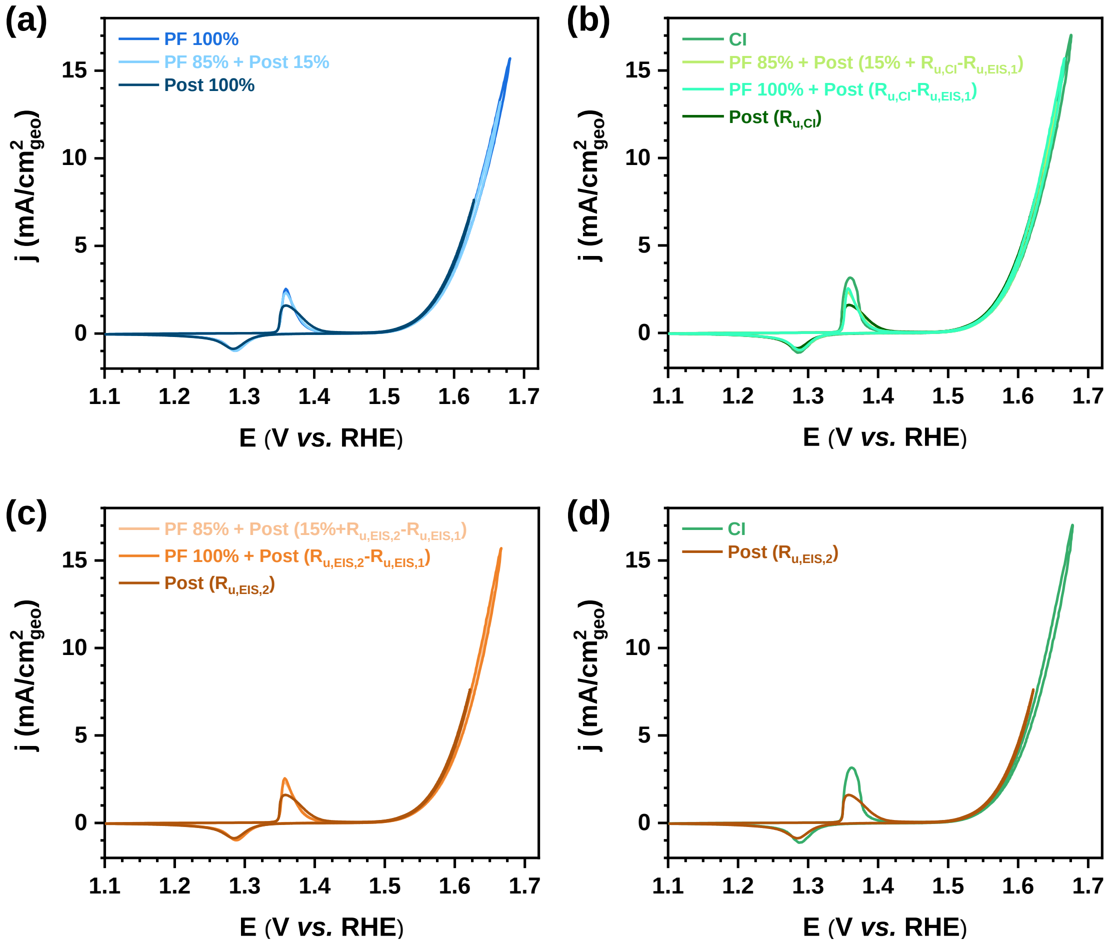

Figure S12. CV curves comparing the OER activity of the NiO$_x$H$_y$/FTO electrode with Type 2 contact impedance in **Figure 2a** using different R_u value options (*i.e.*, $R_{u,EIS,1}$, $R_{u,CI}$, and $R_{u,EIS,2}$) for *iR* compensation: (a) $R_{u,EIS,1}$, (b) $R_{u,CI}$, and (c) $R_{u,EIS,2}$, and (d) comparison of the effects of $R_{u,CI}$, and $R_{u,EIS,2}$ on the *iR*-compensated OER activity. Here, the degree of *iR* compensation is 100%.

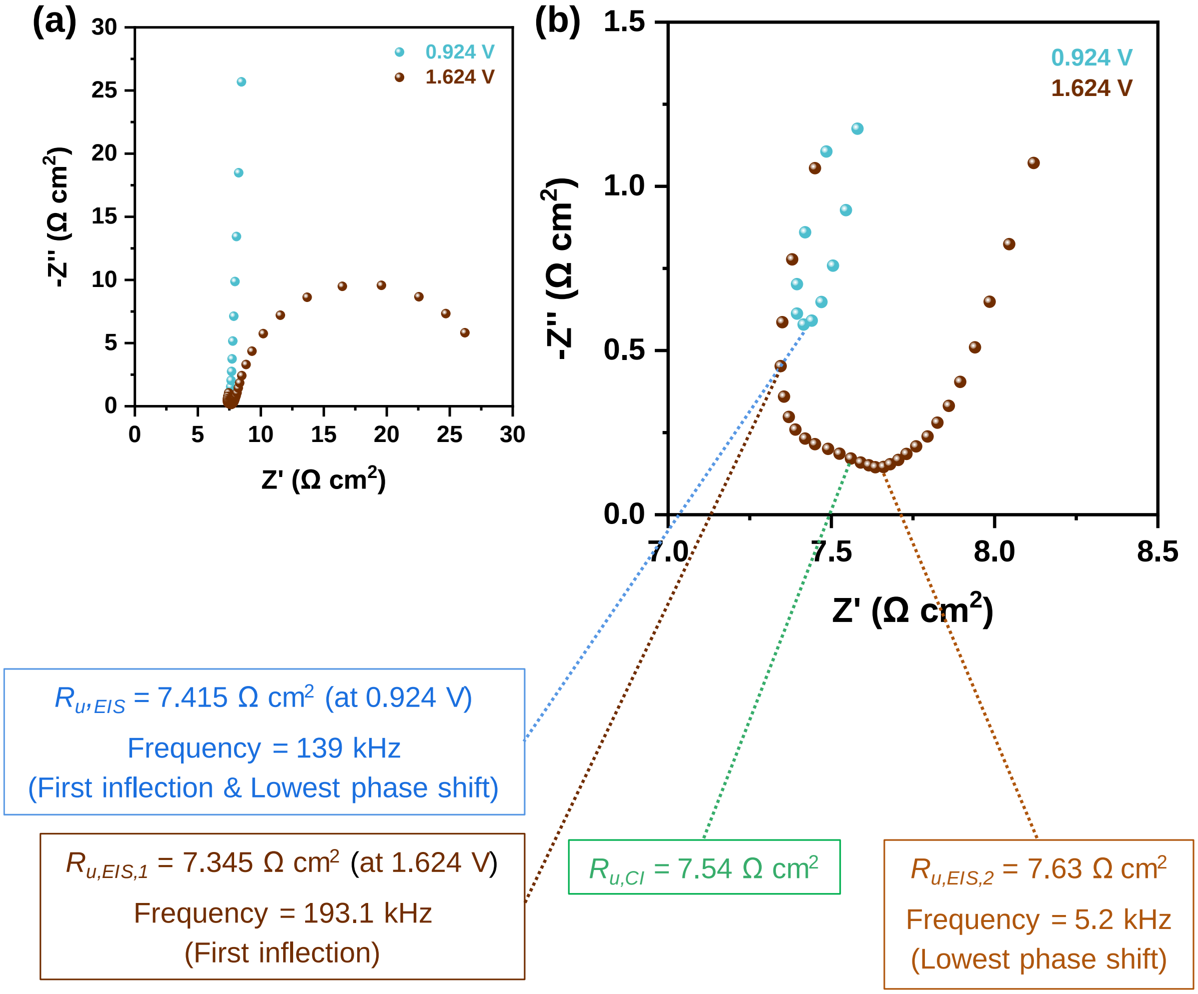

Figure S13. EIS Nyquist plots of the NiO_xH_y/FTO electrode with Type 1 contact impedance. (a) Nyquist plots at 0.924 V and 1.624 V and (b) comparison of possible R_u value options (*i.e.*, $R_{u,EIS,1}$, $R_{u,CI}$, and $R_{u,EIS,2}$) for *iR* compensation.

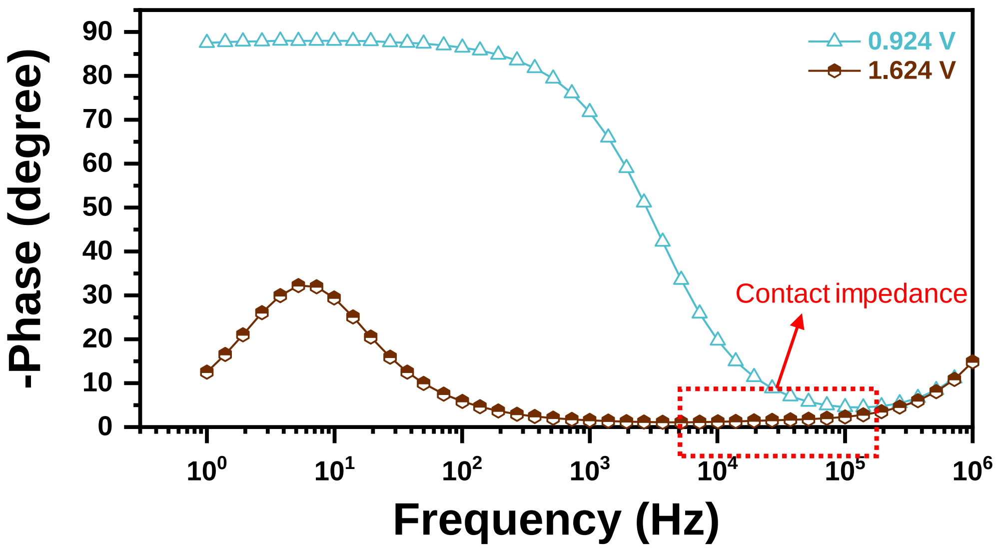

Figure S14. EIS Bode phase plots of the NiO_xH_y/FTO electrode with Type 1 contact impedance at 0.924 V and 1.624 V.

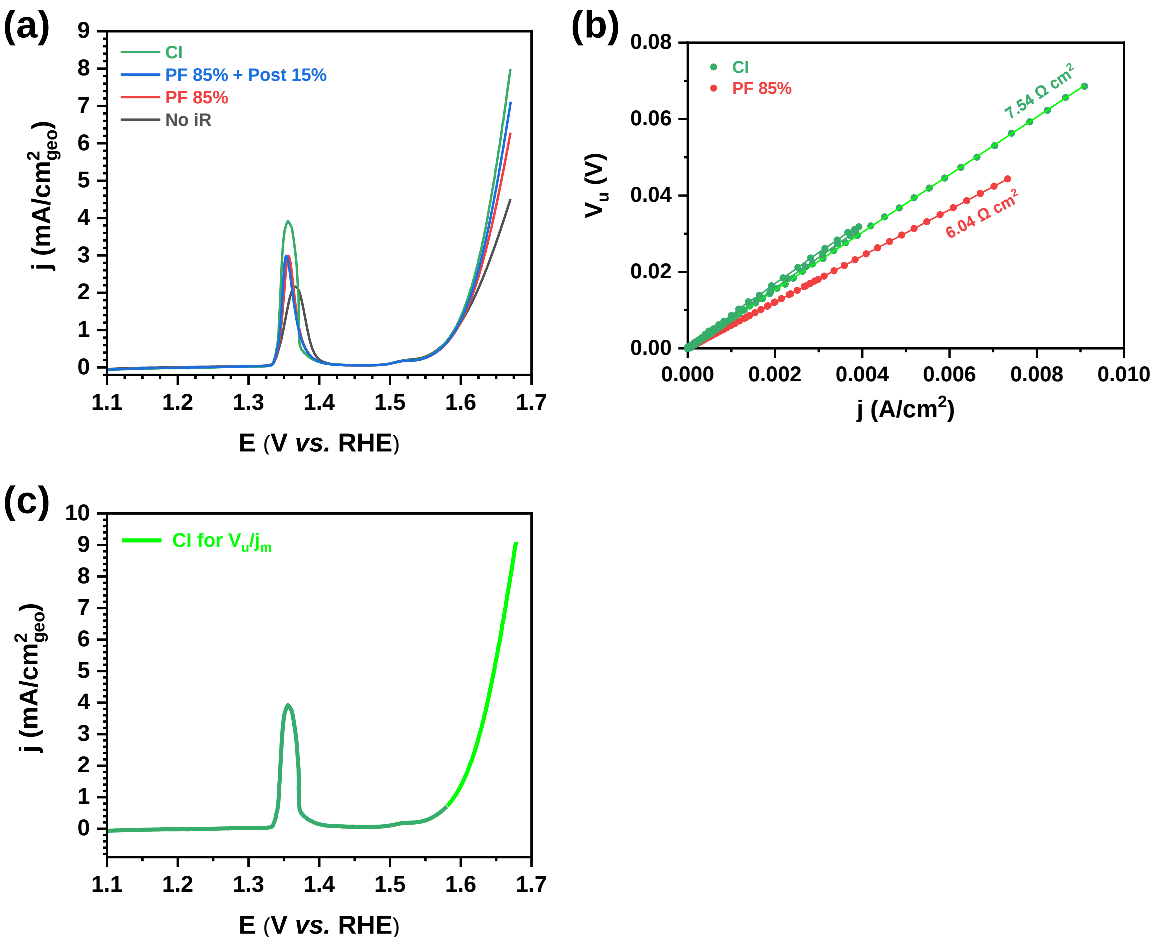

Figure S15. (a) LSV curves at a scan rate of 10 mV/s of the NiO_xH_y/FTO electrode with Type 1 contact impedance employing different methods and degrees of *iR* compensation, (b) plots of V_u *versus* j for CI and PF 85%, and (c) potential and current density region used for $R_{u,CI}$ estimation in the plot of V_u versus j in **Figure S15b**.

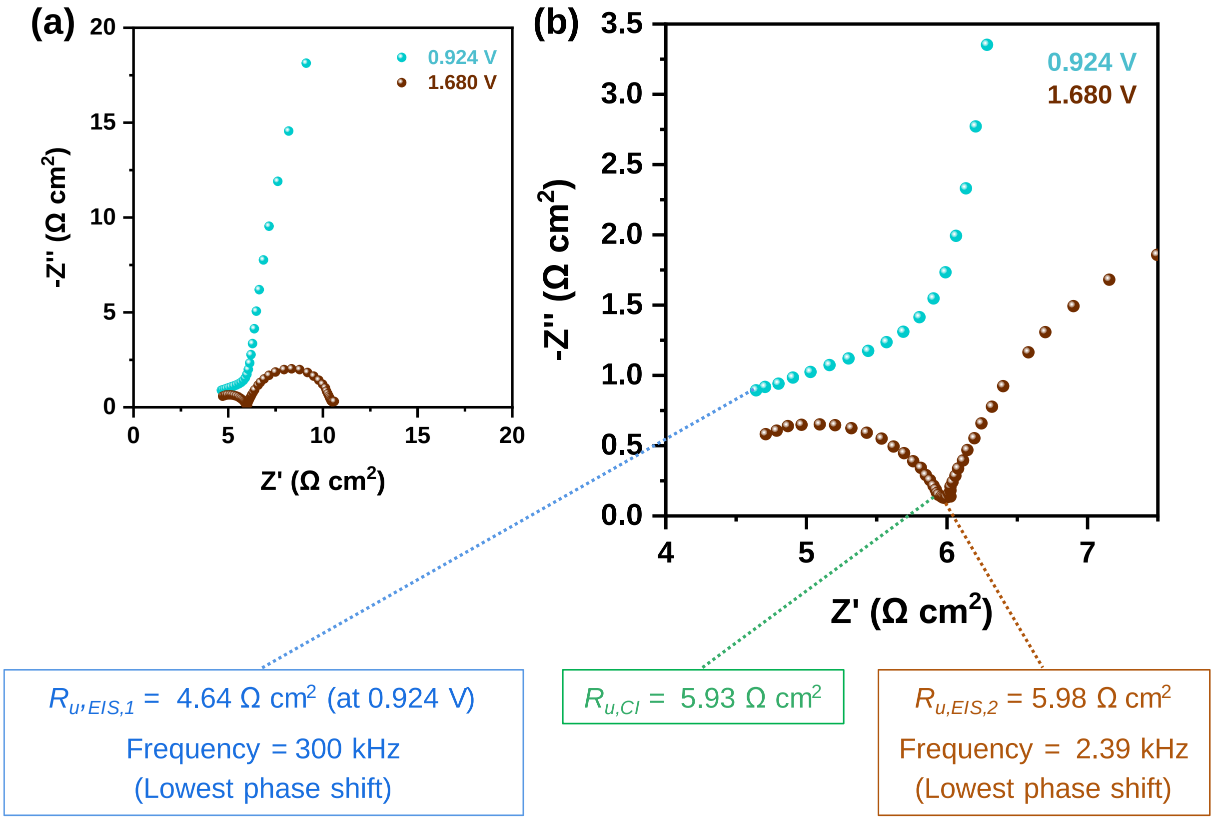

$R_{u,EIS,1}$ = 4.64 Ω cm^2 (at 0.924 V)
Frequency = 300 kHz
(Lowest phase shift)

$R_{u,CI}$ = 5.93 Ω cm^2

$R_{u,EIS,2}$ = 5.98 Ω cm^2
Frequency = 2.39 kHz
(Lowest phase shift)

Figure S16. EIS Nyquist plots of the NiO_xH_y/FTO electrode with Type 3 contact impedance. (a) Nyquist plots at 0.924 V and 1.680 V and (b) comparison of possible R_u value options (*i.e.*, $R_{u,EIS,1}$, $R_{u,CI}$, and $R_{u,EIS,2}$) for *iR* compensation.

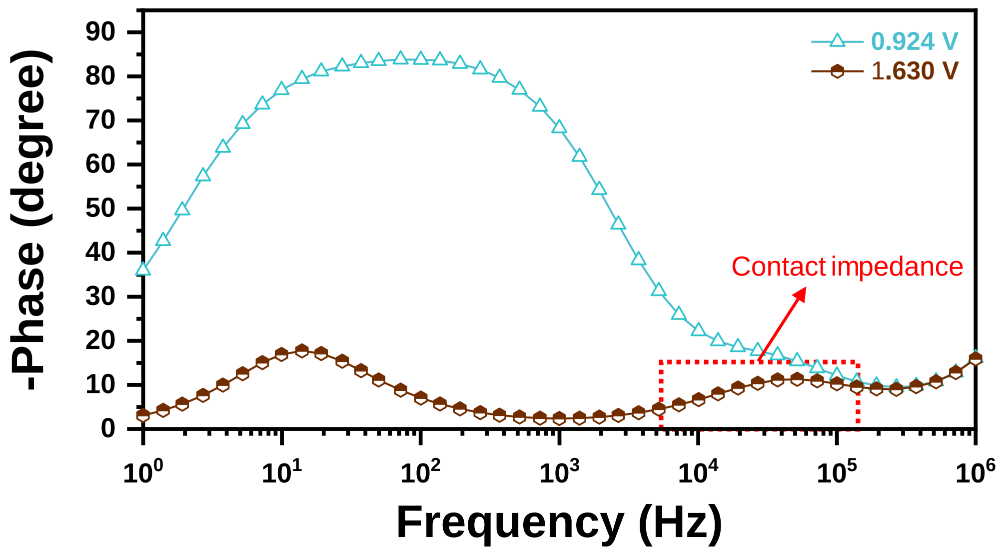

Figure S17. EIS Bode phase plots of the NiO_xH_y/FTO electrode with Type 3 contact impedance at 0.924 V and 1.630 V.

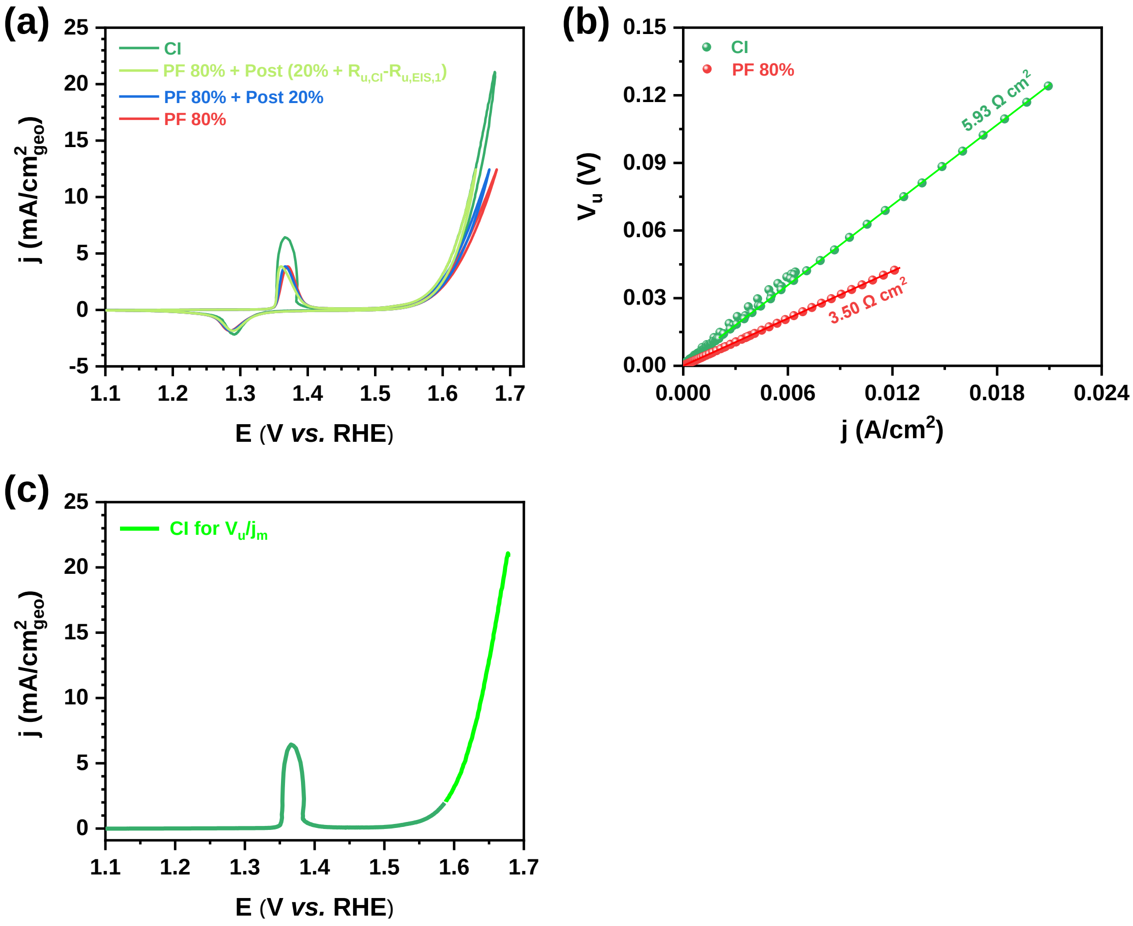

Figure S18. (a) CV curves at a scan rate of 10 mV/s of the NiO_xH_y/FTO electrode with Type 3 contact impedance employing different methods and degrees of *iR* compensation, (b) plots of V_u *versus j* for CI and PF 80%, and (c) potential and current density region used for $R_{u,CI}$ estimation in **Figure S18b**.

2.5. Cautions about EIS-based R_u measurement in the presence of contact impedance

While contact resistance is included as a component of the R_u and can be challenging to distinguish without preparing additional control samples,[5] contact impedance can be differentiated from other components of R_u through potential-dependent EIS analysis. Here, we provide several cautions regarding the measurement of R_u using EIS when contact impedance is present. These cautions are as follows:

(1) *iR* compensation using automatic EIS for R_u measurement reflects the impact of contact impedance on the catalytic performance of electrodes, as $R_{u,auto}$ is approximately equal to $R_{u,EIS,1}$.

(2) $R_{u,EIS,2}$ can be utilized for PF or post *iR* compensation when evaluating the catalytic performance of the catalyst layer and substrate alone, excluding the influence of contact impedance.

(3) $R_{u,auto}$ may vary depending on the shape of the contact impedance observed on the Nyquist plot (or its frequency distribution) and the applied potential during EIS analysis.

(4) Specifying $R_{u,EIS,1}$ may become ambiguous under OER potentials when there is an overlap between contact impedance and roll-off phenomena caused by offsets during potentiostat instrument calibration or artifacts introduced by the test fixture, such as cable bending.

These considerations highlight the importance of carefully interpreting R_u measurements in the presence of contact impedance, taking into account the potential-dependent behavior and potential sources of measurement artifacts.

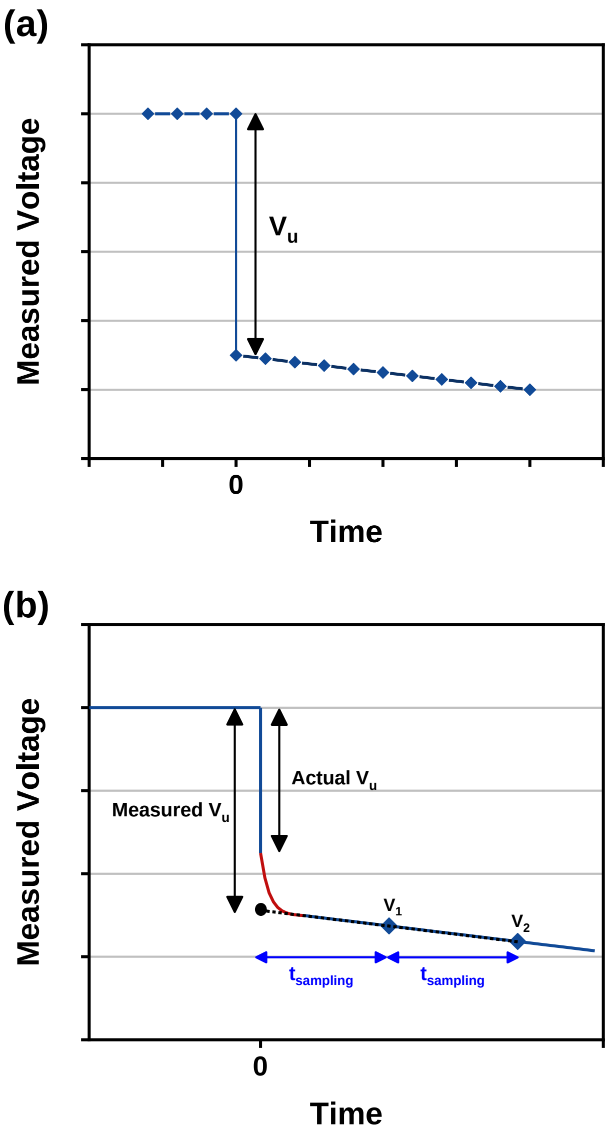

Figure S19. Illustrations for explaining the principle of V_u (= iR_u) measurement during CI (a) in the ideal case without contact impedance and (b) in the presence of contact impedance with the one-tenth of RC time constant sufficiently small compared to $t_{sampling}$.

Table S2. Electrochemical parameters obtained by fitting the EIS data of the NiO_xH_y/FTO electrode in **Figures S16** and **S17** with Type 3 contact impedance at the electrode connector/substrate interface using the Equivalent circuit in **Figure S10b**.

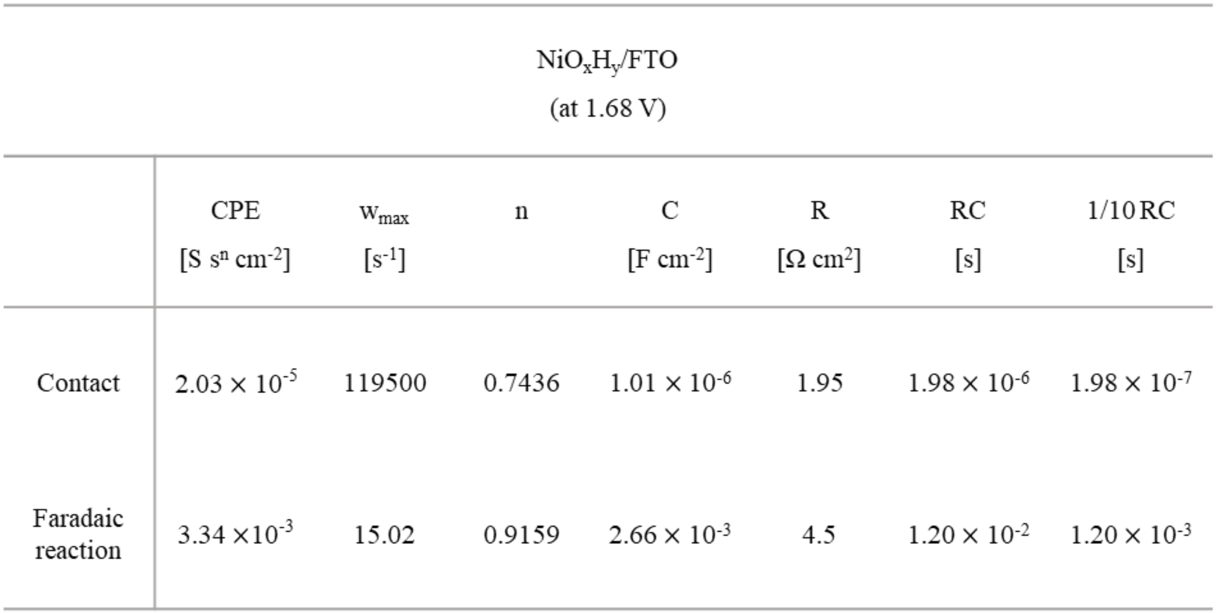

	NiO_xH_y/FTO (at 1.68 V)						
	CPE [$S\ s^n\ cm^{-2}$]	w_{max} [s^{-1}]	n	C [$F\ cm^{-2}$]	R [$\Omega\ cm^2$]	RC [s]	1/10 RC [s]
Contact	2.03×10^{-5}	119500	0.7436	1.01×10^{-6}	1.95	1.98×10^{-6}	1.98×10^{-7}
Faradaic reaction	3.34×10^{-3}	15.02	0.9159	2.66×10^{-3}	4.5	1.20×10^{-2}	1.20×10^{-3}

2.6. Failure of CI in the presence of contact impedance

Figure S19a illustrates the process of R_u measurement using current interruption for an ideal electrochemical system without any contact impedance, which employs the equivalent circuit model in **Figure S10a**. During current interruption, there is a sudden voltage drop caused by the series resistance within the electrochemical system. Following this voltage drop, the potential slowly decreases due to the capacitive charging or discharging of the large faradaic capacitance present in the electrochemical system. By performing a linear fitting of the data points of the measured potentials on this capacitive charging or discharging curve, it is possible to extrapolate the potential at time zero (0 s) when the current interruption occurs. By comparing the potential before current interruption with the extrapolated potential at 0 s, the voltage drop (V_u) can be estimated. R_u, which represents the series resistance of the electrochemical system, can be obtained according to the equation $V_u = iR_u$. Note that an appropriate relationship between the sampling time for potential data points during the current interruption ($t_{sampling}$) and the characteristics decay time of the electrochemical system (*i.e.*, RC time constant = $1/w_{max}$) is required to achieve accurate

R_u measurement through current interruption. Specifically, accurate R_u measurement is achieved when $t_{sampling}$ is approximately one-tenth of the RC time constant.[6]

On the other hand, the R_u measurement using current interruption may encounter issues in the presence of contact impedance with a very small RC time constant. In **Supporting Note 2.3**, it is explained that the contact impedance has a smaller RC time constant compared to the faradaic impedance. Nevertheless, as long as one-tenth of the RC time constant of the contact impedance is similar to or greater than $t_{sampling}$, current interruption can still yield precise R_u measurement. However, if one-tenth of the RC time constant of the contact impedance is sufficiently smaller than $t_{sampling}$, R_u measurement using current interruption can lead to incorrect results. The illustration in **Figure S19b** explains how R_u measurement by current interruption can fail in the presence of contact impedance with a sufficiently small RC time constant. The red curve in **Figure S19b** depicts a rapid potential drop caused by the contact impedance. This potential drop occurs at a rate faster than $t_{sampling}$ due to a sufficiently small RC time constant for the contact impedance. As a consequence, this leads to an overestimation of the measured V_u compared to actual V_u when extrapolating the potential at 0 s based on linear fitting of the measured potential data points on the capacitive charging or discharging curve.

To assess whether the contact impedance can affect the accuracy of current interruption, it is necessary to determine the RC time constant specific to the electrochemical system and compare it with $t_{sampling}$. For the NiO_xH_y/FTO electrode with Type 3 contact impedance at the electrode holder/substrate interface in **Figure S16-S18**, the RC time constants were calculated based on electrochemical parameters obtained by fitting the EIS data (**Table S2**). Here, Type 3 contact impedance was selected for easier EIS fitting due to its distinct semicircle shape compared to Type 1 and Type 2 contact impedance. The RC time constant of the contact impedance was found to be significantly smaller (10,000 times) compared to the faradaic reaction (*e.g.*, OER). This substantial difference arises from the extremely small capacitance at the electrode holder/substrate interface in comparison to the electrochemical double layer at the catalyst/electrolyte interface. This discrepancy is not only because the contact area between the electrode holder and substrate is smaller than the active geometric area of the catalytic electrode, but also because the electrochemical surface area is significantly larger than the geometric area due to the surface roughness and electrolyte permeability of the catalyst layer. As a result, the one-tenth of the RC time constant for the contact impedance was determined to be 0.198 μs, which is considerably smaller than the t_{sampling} of 50 μs employed in the experiments discussed in this Viewpoint. This finding indicates that the contact impedance at the electrode holder/substrate interface can lead to inaccurate measurement of R_u using current interruption. Additionally, it is worth noting that reducing the value of t_{sampling} below one-tenth of the RC time constant of the contact impedance is not a viable solution for avoiding the overestimation issue of $R_{\text{u,CI}}$ in the presence of contact impedance. This is because when t_{sampling} becomes excessively small, the current interruption process is significantly influenced by cable capacitance, leading to more erroneous R_{u} measurements.[6]

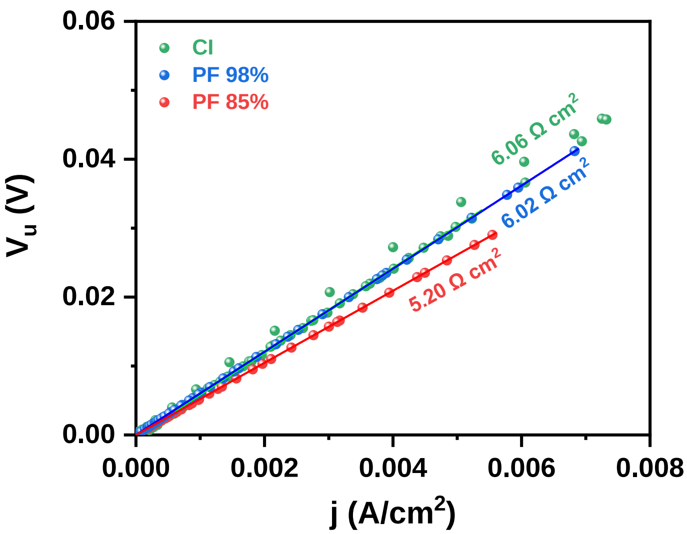

Figure S20. Plots of V_u versus j for the NiO_xH_y/FTO electrode in **Figure 2b** without contact impedance.

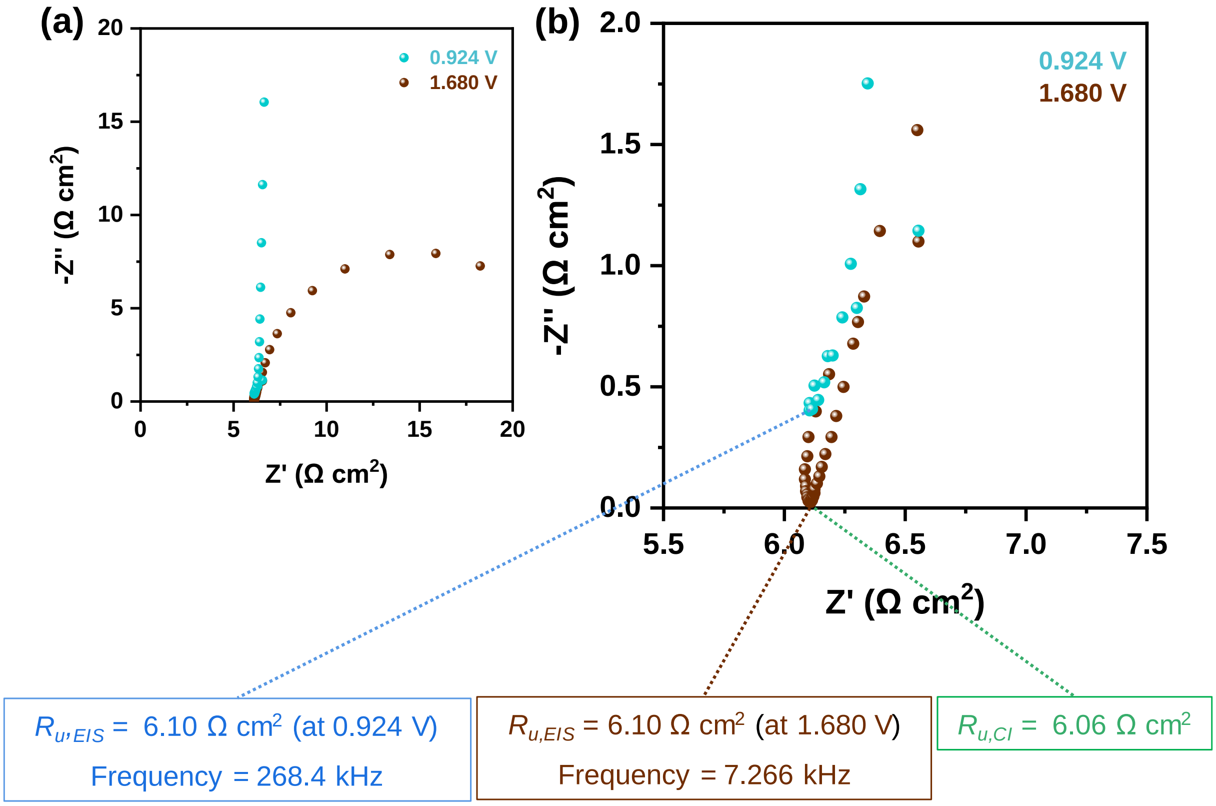

$R_{u,EIS}$ = 6.10 Ω cm^2 (at 0.924 V)
Frequency = 268.4 kHz

$R_{u,EIS}$ = 6.10 Ω cm^2 (at 1.680 V)
Frequency = 7.266 kHz

$R_{u,CI}$ = 6.06 Ω cm^2

Figure S21. EIS Nyquist plots of the NiO_xH_y/FTO electrode in **Figure 2b** without contact impedance before the OER testing. Panel b is a magnified image of panel a.

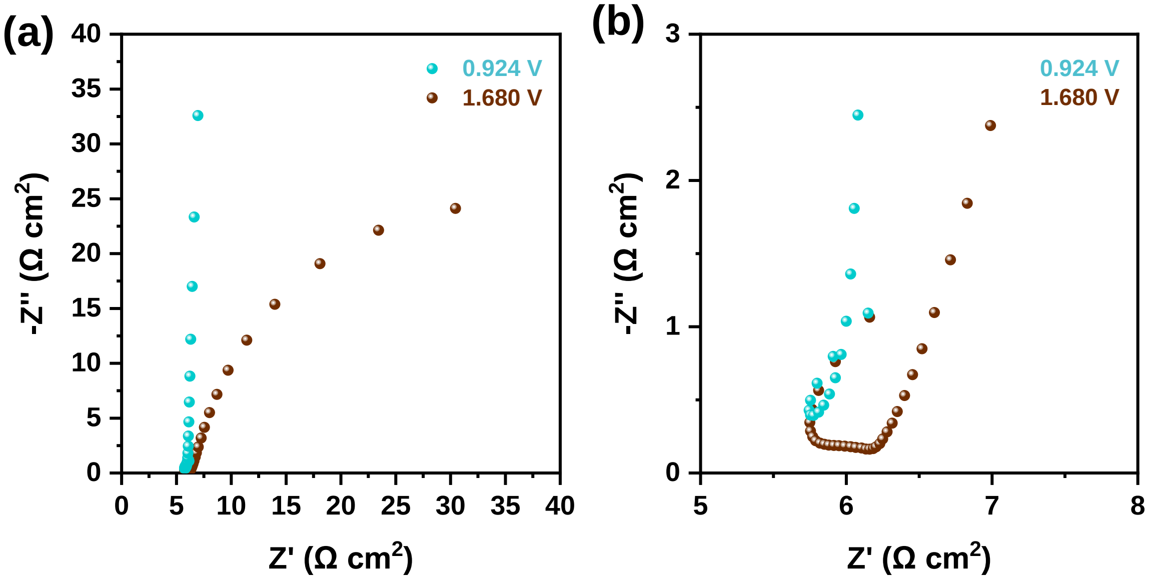

Figure S22. EIS Nyquist plots of the NiO_xH_y/FTO in **Figure 2b** after the OER testing.

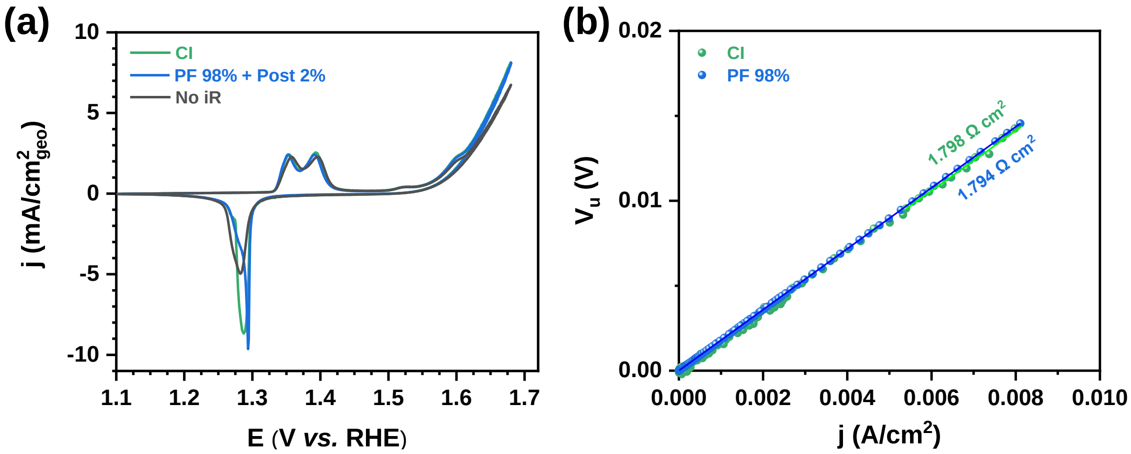

Figure S23. (a) CV curves at a scan rate of 10 mV/s of CV-activated Ni foil (Ni-CV) electrode and (b) plots of V_u versus j for CI and PF 98%. Here, the Ni-CV electrode consists of an *in situ*-formed NiO_xH_y layer on the Ni foil substrate.

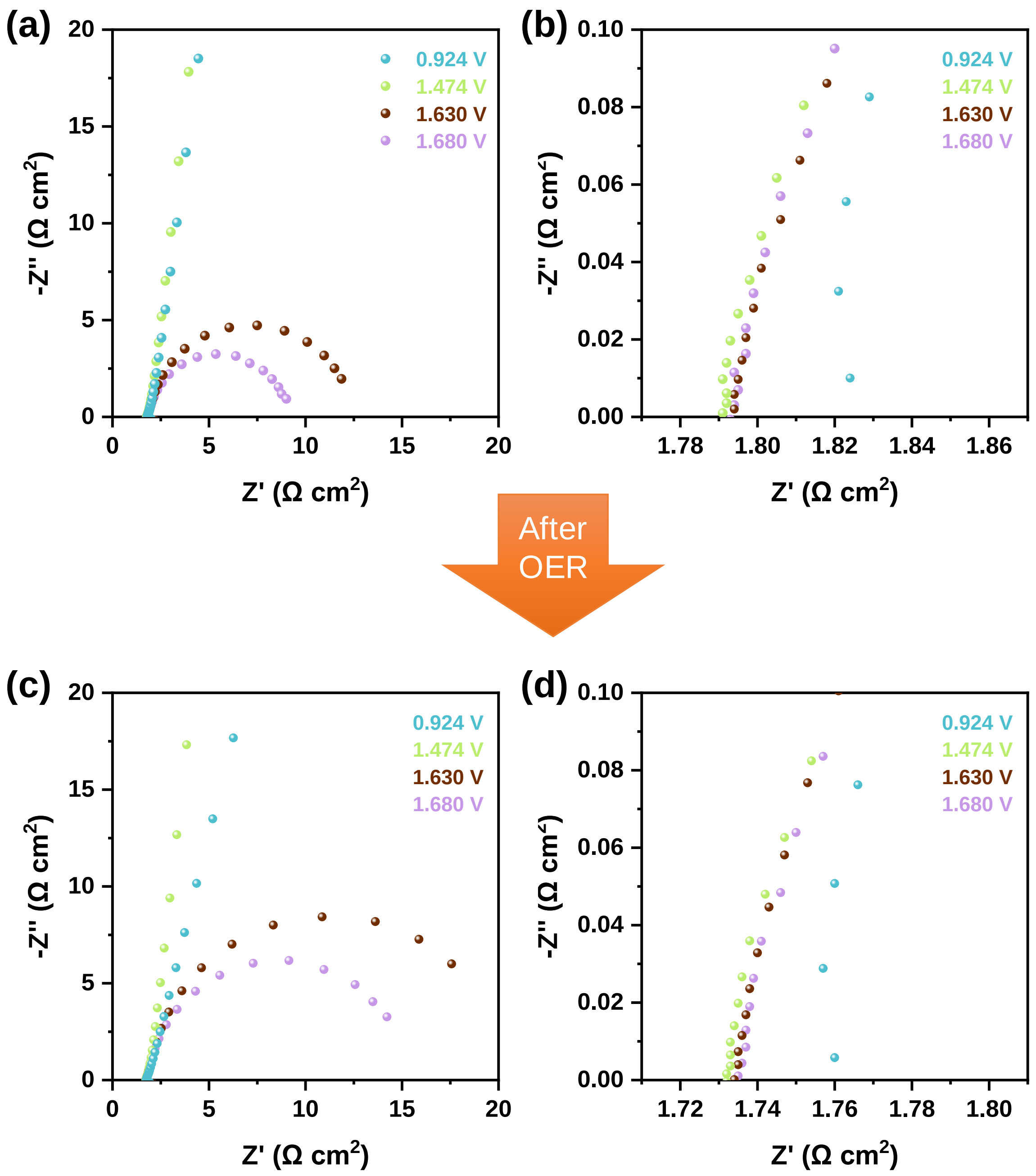

Figure S24. EIS Nyquist plots of the Ni-CV electrode without contact impedance at both electrode holder/substrate and substrate/catalyst interfaces (a,b) before and (c,d) after the OER testing.

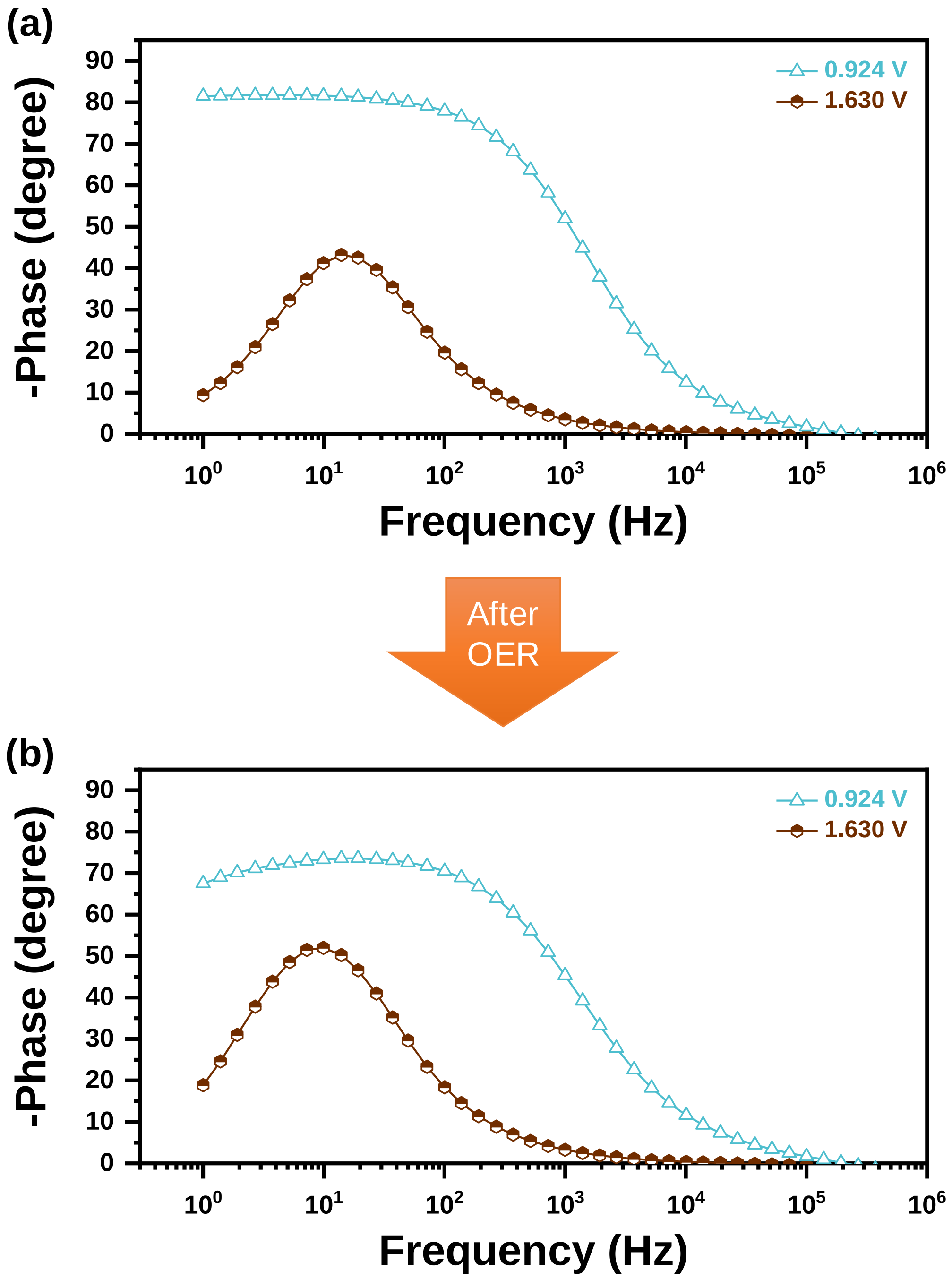

Figure S25. EIS Bode phase plots of the Ni-CV electrode without contact impedance at both electrode holder/substrate and substrate/catalyst interfaces (a,b) before and (c,d) after the OER testing.

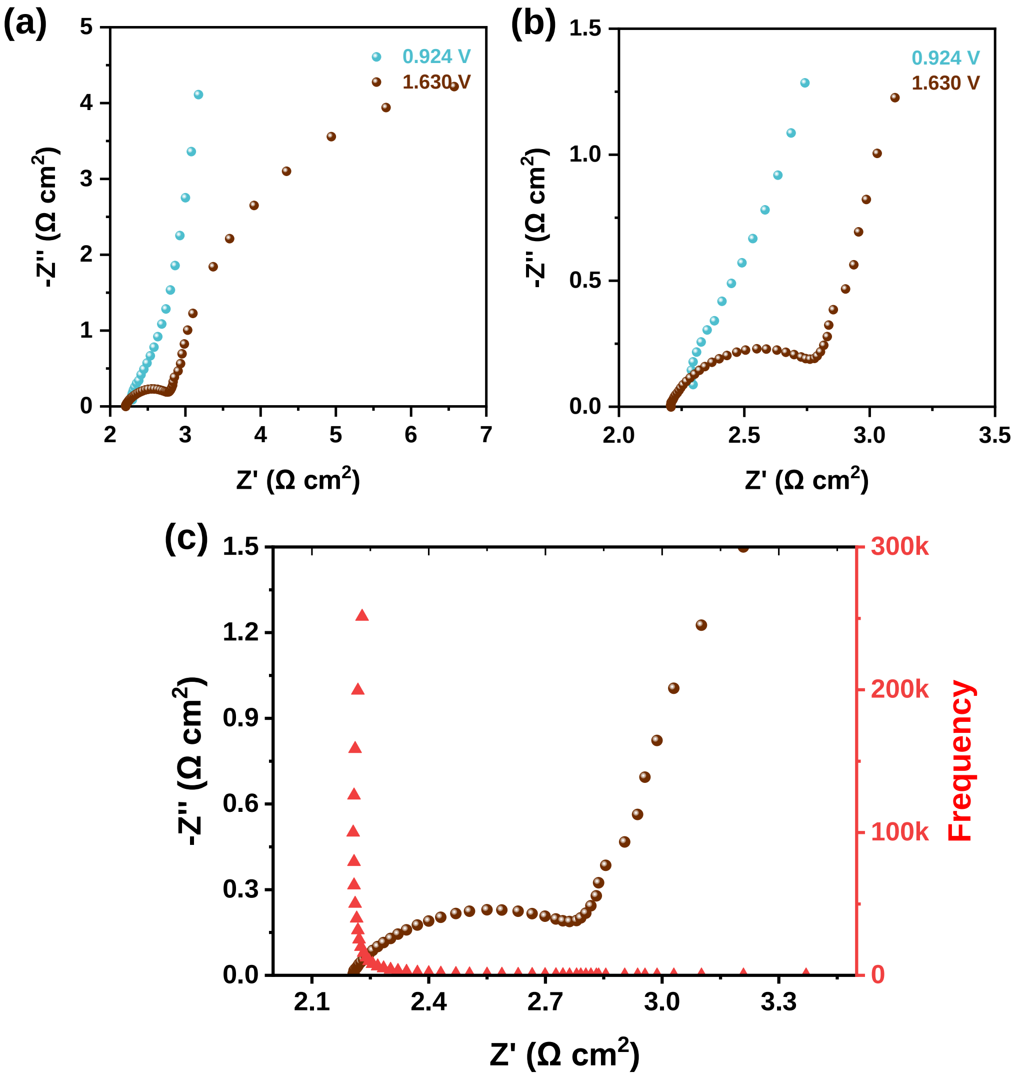

Figure S26. EIS data of the NiO_xH_y/Ni foil electrode connected with the Pt clip: (a,b) Nyquist plots at 0.924 (non-faradaic potential) and 1.630 V (OER potential), and (c) Nyquist plot at 1.630 V with the frequency distribution of the EIS data.

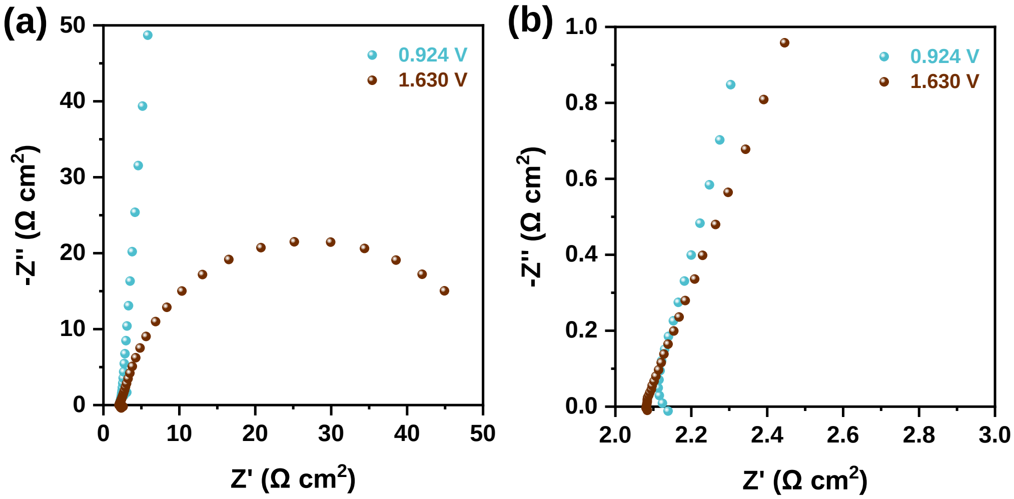

Figure S27. EIS Nyquist plots of the NiO_xH_y/Ni foil electrode connected with the Pt clip after completely peeling off the NiO_xH_y layer from the Ni foil substrate.

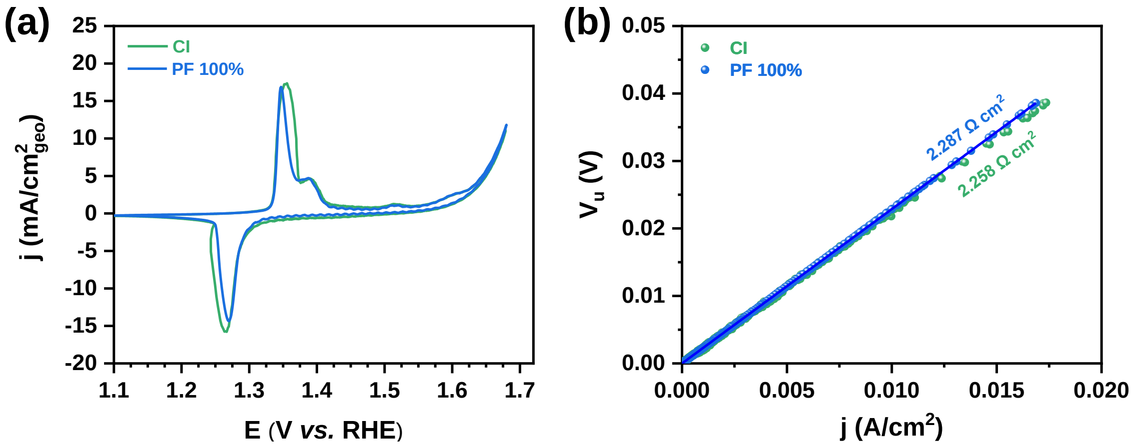

Figure S28. (a) CV curves at a scan rate of 10 mV/s of the NiO_xH_y/Ni foil electrode connected with the Pt clip in **Figure S26** and (b) plots of V_u versus j for CI and PF 100%.

Table S3. Electrochemical parameters obtained by fitting the EIS data of the NiO_xH_y/Ni foil electrode in **Figure S26a-c** with contact impedance at the substrate/catalyst interface using the equivalent circuit in **Figure S10b**.

	NiO_xH_y/Ni foil-Pt clip (at 1.63 V)						
	CPE [S s^n cm^{-2}]	w_{max} [s^{-1}]	n	C [F cm^{-2}]	R [Ω cm^2]	RC [s]	1/10 RC [s]
Contact	2.72×10^{-3}	998.3	0.7436	4.63×10^{-4}	0.627	2.90×10^{-4}	2.90×10^{-5}
Faradaic reaction	2.18×10^{-2}	0.633	0.9583	2.22×10^{-2}	11.62	2.58×10^{-1}	2.58×10^{-2}

2.7. Contact impedance at the substrate/catalyst interface

A self-supported electrode can be simply prepared by subjecting Ni foil to 2000 cycles of CV electrochemical conditioning, which is denoted as Ni-CV. This process leads to *in situ* formation of a thick NiO_xH_y layer on the Ni foil substrate. The Ni-CV electrode exhibits comparable OER activity and R_u values when using PF and CI methods (**Figure S23**). Furthermore, there were no discernible differences in the shape of the EIS spectra of the Ni-CV electrode before and after OER testing. This suggests that contact impedance was not developed even after the OER testing potentially due to the strong adhesion and good contact between the *in situ*-grown NiO_xH_y catalyst layer and the Ni foil substrate (**Figure S24** and **S25**).

Apart from contact impedance, note that the $R_{u,EIS}$ values at potentials above the anodic redox reaction potential of $Ni^{2+/3+}$ (*e.g.*, 1.474, 1.630, and 1.680 V) were lower than the $R_{u,EIS}$ at 0.924 V. This is attributed to the conductivity enhancement of the catalyst layer during the phase transformation of the insulating $Ni(OH)_2$ (Ni^{2+}) to the conductive NiOOH (Ni^{3+}).[2,7] The change in $R_{u,EIS}$ caused by potential-dependent R_{et} becomes detectable as the R_{et} across the catalyst layer becomes significant, which occurs when the thickness of the NiO_xH_y catalyst layer increases to a sufficient extent. Additionally, differences in peak shape and peak current density for the $Ni^{2+/3+}$ redox reaction of the electrode were observed between CI and PF methods in **Figure S23**a.

The NiO_xH_y/Ni foil electrode connected with a Pt clip does not exhibit contact impedance at the electrode holder/substrate interface. This is because Pt does not form a surface oxide layer, and the Ni foil was electropolished prior to use to eliminate any surface oxide layers. However, the NiO_xH_y/Ni foil electrode displayed contact impedance in the high-frequency region of the EIS Nyquist plot (**Figure S26**). Notably, this contact impedance disappeared when the NiO_xH_y catalyst layer was peeled off from the Ni foil substrate (**Figure S27**). These results identify the presence of contact impedance at the interface between the NiO_xH_y catalyst layer and the Ni foil substrate. **Figure S28** shows that the NiO_xH_y/Ni foil electrode displays identical OER activity and R_u values, regardless of using the CI and PF 100% methods. This equivalence is observed despite the presence of contact impedance at the substrate/catalyst interface. Therefore, it can be inferred that the contact impedance at the substrate/catalyst interface does not hinder the accurate measurement of R_u using the CI method, unlike the contact impedance at the electrode holder/substrate interface. To comprehend this disparity, the RC time constants were calculated and presented in **Table S3**. Despite the contact impedance at the substrate/catalyst interface having a significantly smaller RC time constant (1000 times) compared to the faradaic impedance, one-tenth of the RC time constant for the contact impedance was found to be 29 μs, which is sufficiently high to be comparable to the $t_{sampling}$ of 50 μs. This similarity in values would enable the acquisition of potential data points during current interruption from the capacitive charging or discharging curve of the contact impedance, rather than the faradaic impedance, thereby avoiding any overestimation of V_u.

In summary, the difference between the two types of contact impedance at electrode holder/substrate and substrate/catalyst interfaces is attributed to the higher RC time constant of the contact impedance at the substrate/catalyst interface compared to the electrode holder/substrate. This difference arises from the larger capacitance at the substrate/catalyst interface, which is a result of the larger geometric active area and surface roughness of the catalytic electrode in contrast to the smaller contact area and flat surface at the electrode holder/substrate interface. Overall, this quantitative estimation of the RC constant provides a clear explanation for why the CI method does not lead to inaccurate measurement of R_u in case of contact impedance at the substrate/catalyst interface.

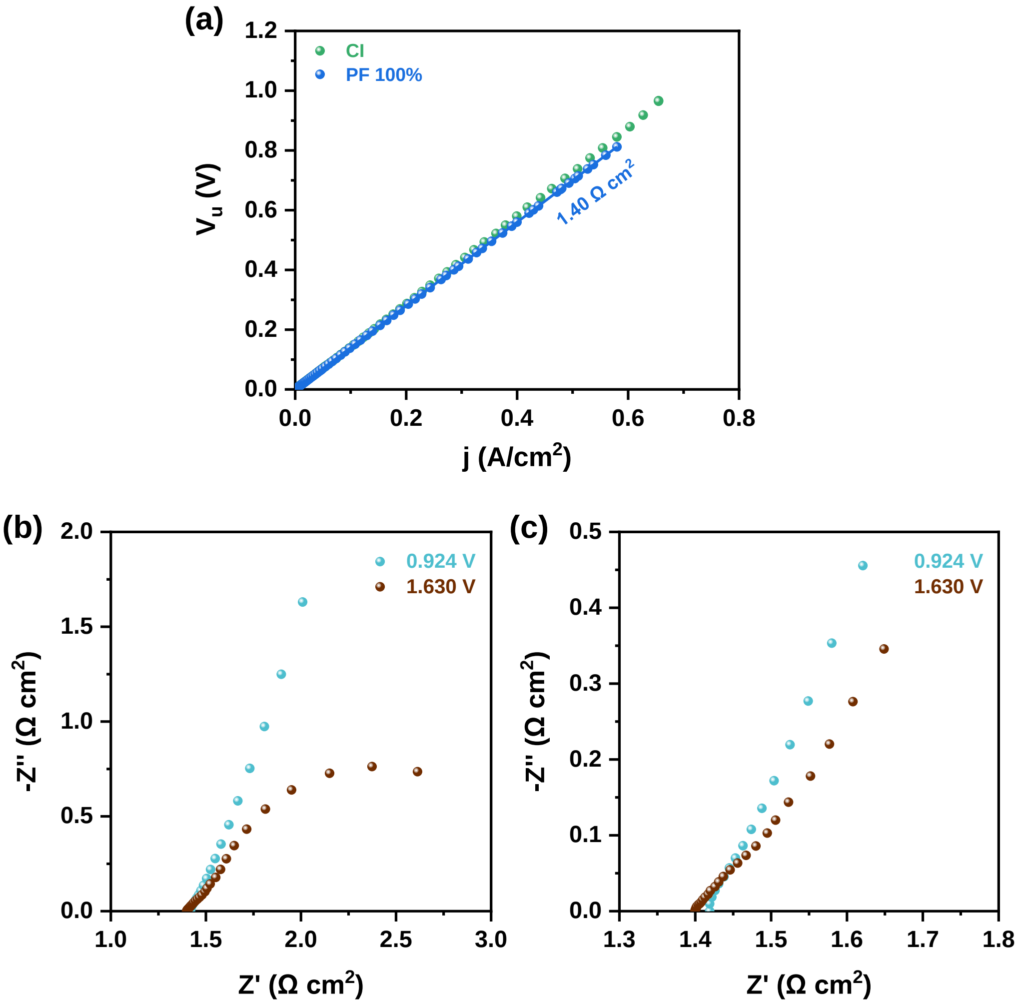

Figure S29. Estimation of R_u value used for the nanoporous NiO_xH_y/Ni foam electrode in **Figure 2d**. (a) The plot of V_u *versus* j for PF 100% and (b,c) EIS Nyquist plots at 0.924 V and 1.630 V.

Supporting Note 3. Varying R_u

3.1. Electrode properties of nanoporous NiO_xH_y/Ni foam related to R_{et} measurement

According to the reference, the R_u of a porous electrode does not include the R_{et} through the porous catalyst layer because the conductive substrate comes into direct contact with the electrolyte.[5,7,8] However, the observation of potential-dependent R_{et} variation in the nanoprous NiO_xH_y/Ni foam electrode suggests the presence of a compact NiO_xH_y layer between the metallic Ni foam substrate and the nanoporous NiO_xH_y layer that prevent the Ni foam substrate from contacting the electrolyte directly. This compact NiO_xH_y layer enable the detection of R_{et} variation of the NiO_xH_y layer with the applied potential.

3.2. Characteristics and limitations of EIS and current interruption for measuring the varying R_u

The potential-dependent EIS analysis allows for the differentiation of R_u variation by potential-dependent R_{et}. Additionally, when EIS is conducted at potentials above the anodic redox reaction of $M^{2+/3+}$, the R_u measurement can reflect the R_{et} of the actual catalytic active phase (MOOH) during the OER. On the other hand, the presence of R_{bubble} may not be reflected in the R_u measured by EIS at OER potentials, as shown in **Figure S29**. This is because a certain amount of OER operation time is required to observe a noticeable impact of the accumulated oxygen bubble near the OER catalytic electrode on the R_u value.[5] However, $R_{u,EIS}$ is measured at a high-frequency region during the EIS analysis, indicating a rapid measurement process. Furthermore, EIS measurement typically starts from high frequencies where the R_u is measured and moves towards lower frequencies. As a result, the duration of the OER operation is not long enough for the measured R_u to be affected by oxygen gas bubbles. Moreover, it is common practice to conduct EIS analysis for R_u measurement before conducting OER testing to use the obtained R_u value for *iR* compensation. This explains why the R_u obtained from EIS analysis typically reflects the R_u variation due to R_{et}, but not R_{bubble}.

The current interruption method has the advantage that it can measure R_u *in situ* during electrochemical analysis. Therefore, it can effectively track the *in situ* variation of R_u caused by R_{bubble} during the OER, as well as reflect the R_{et} of the catalytic active phase (MOOH) during the

OER in R_u. However, it is difficult to measure R_u variation caused by R_{et} using current interruption. To measure R_u variation by R_{et}, it is necessary to compare the R_u before and after the redox reaction of $M^{2+/3+}$. Unfortunately, during potentiodynamic analysis, the current variation before the anodic redox reaction of $M^{2+/3+}$ is too small to perform reliable fitting for the V_u *versus* j plot. Therefore, obtaining a reliable R_u value from the slope of V_u *versus* j plot is not feasible.

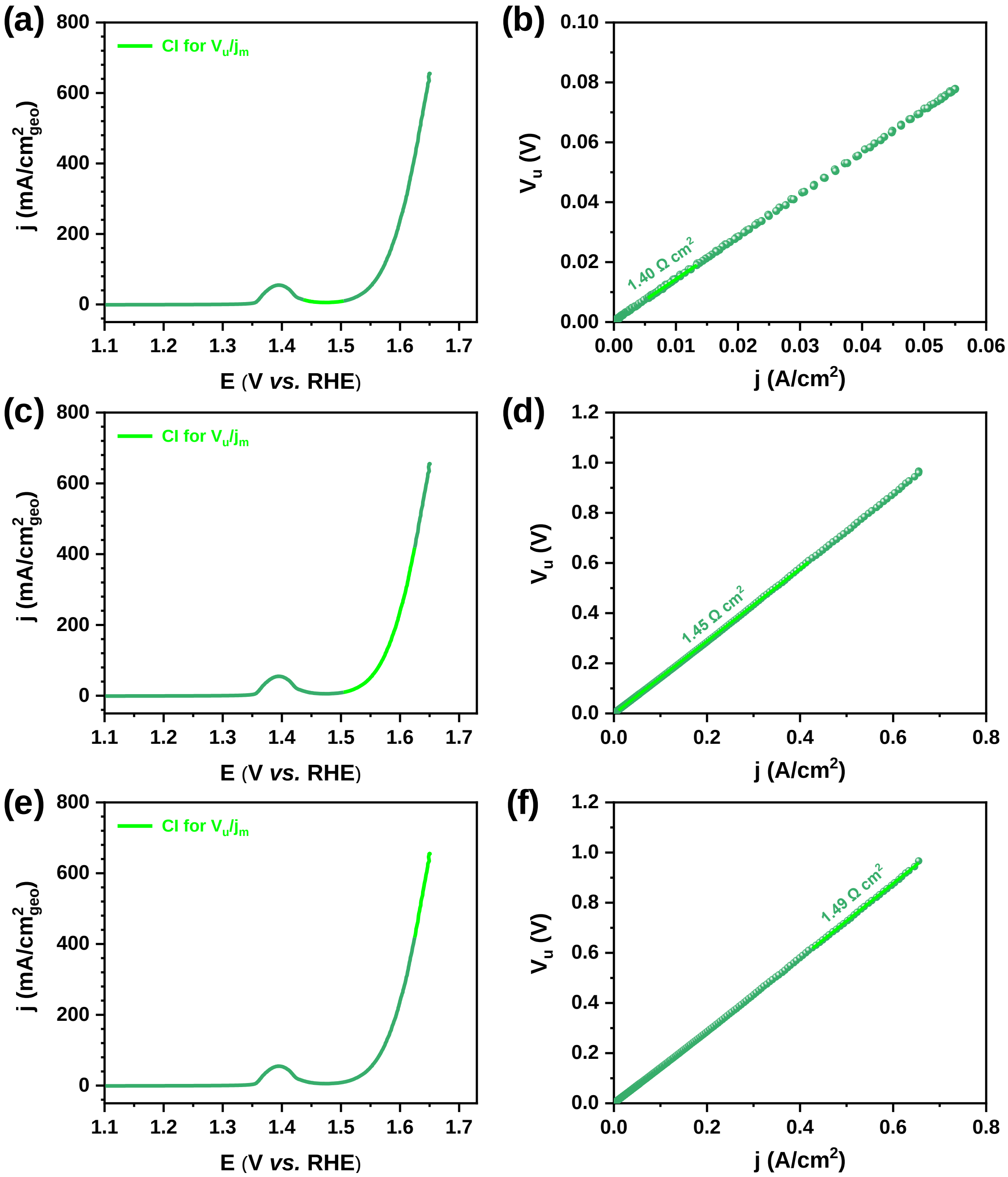

Figure S30. Estimation of $R_{u,CI}$ for the nanoporous NiO_xH_y/Ni foam electrode in **Figure 2c**. (a,c,e) forward scans of CV curve highlighting different *j* range and (b,d,e) plots of V_u versus *j* corresponding to the highlighted *j* ranges, respectively: (a,b) at low *j*, (c,d) at medium *j*, and (e,f) at high *j*. Here, $R_{u,CI}$ value changes with *j* value.

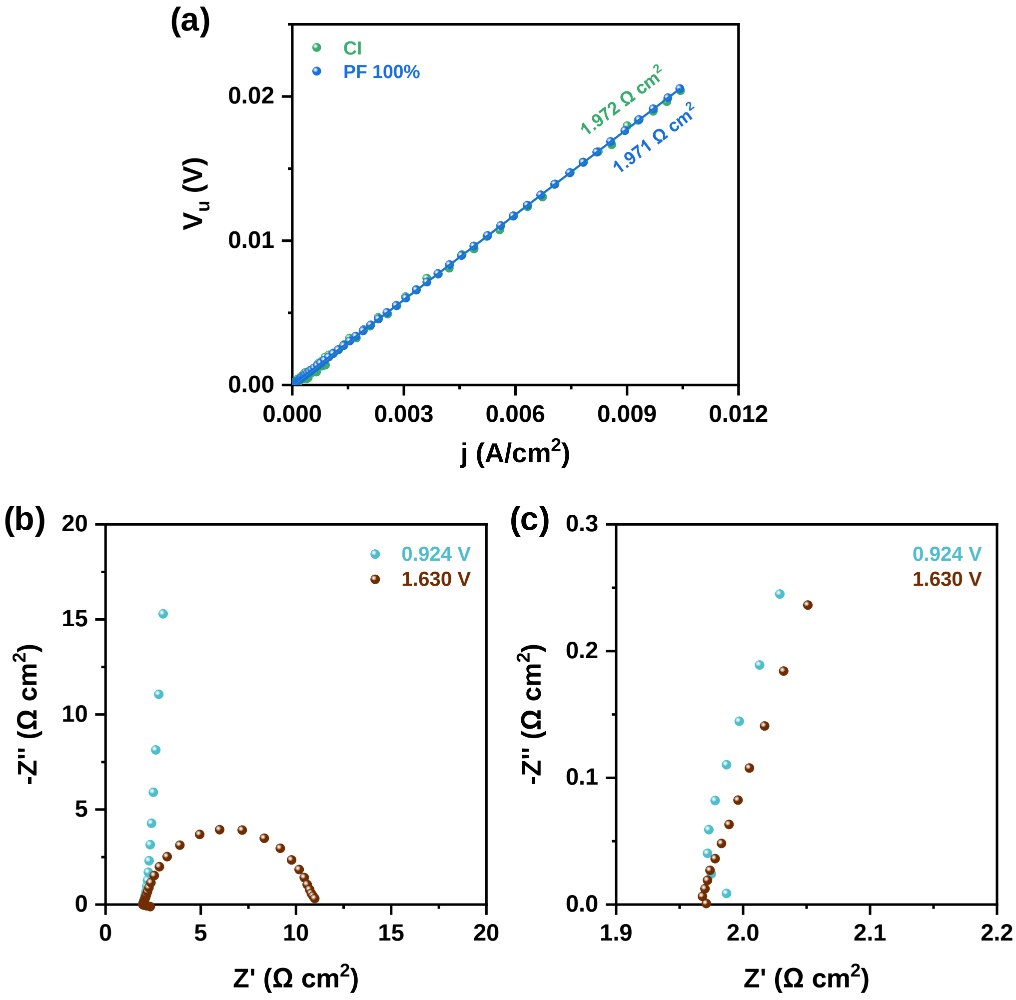

Figure S31. Estimation of R_u values used for Ni foil in **Figure 2d**. (a) The plots of V_u *versus* j and (b,c) Nyquist plots at 0.924 and 1.630 V.

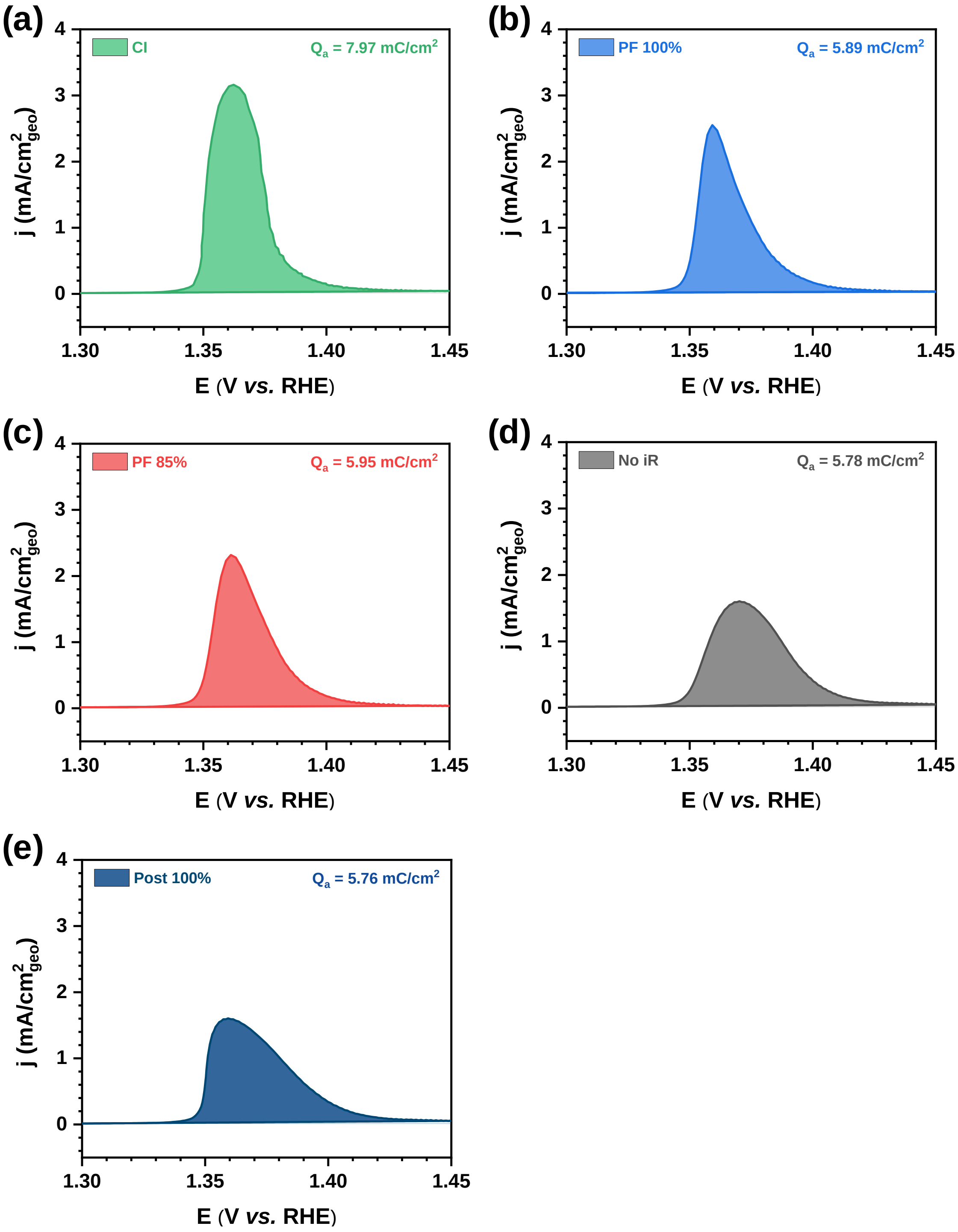

Figure S32. Integration of anodic redox peak for $Ni^{2+/3+}$ to estimate the Q_a of the NiO_xH_y/FTO electrode employing different methods and degrees of *iR* compensation in **Figures 2a** and **3a**.

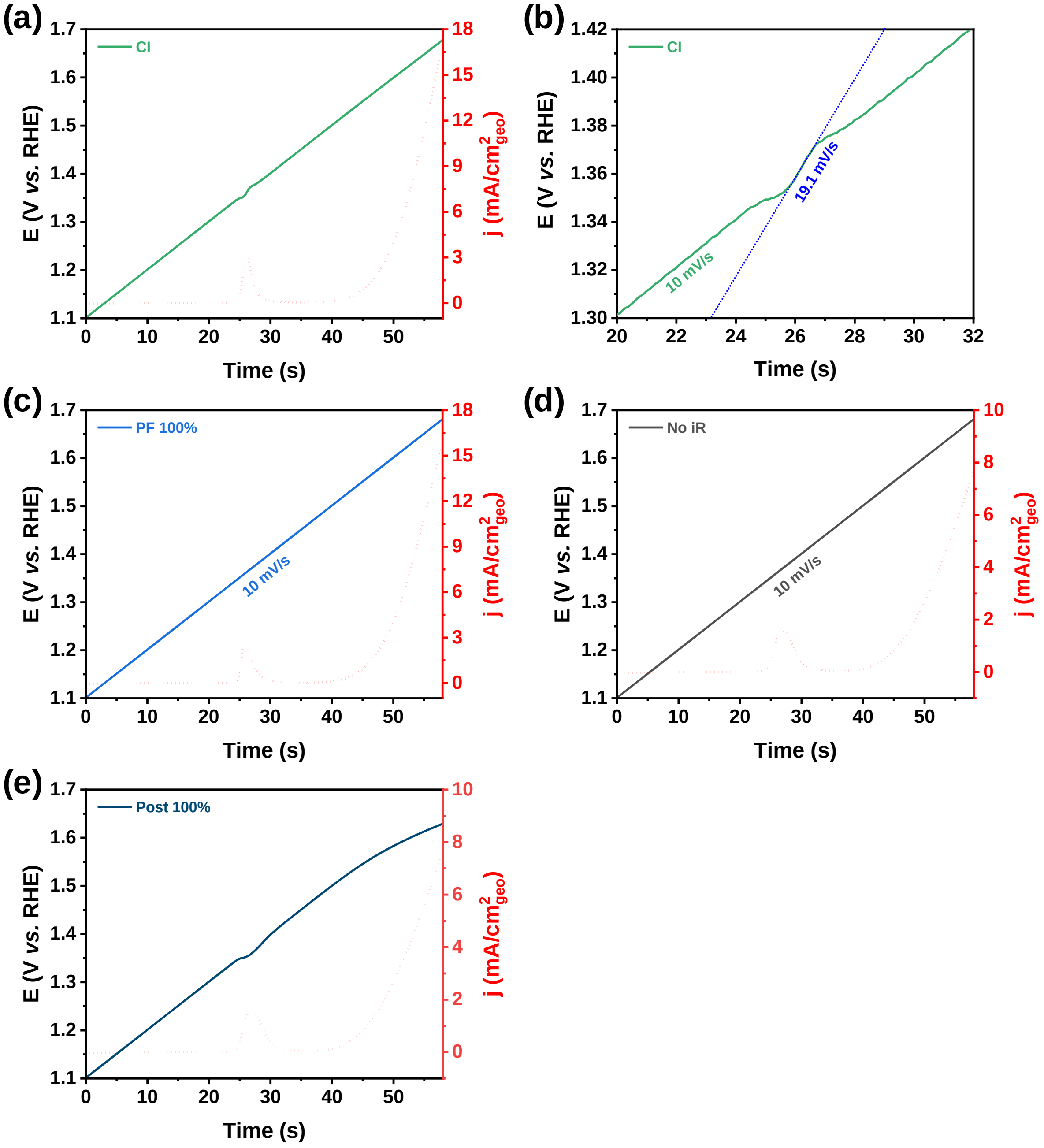

Figure S33. Plots of applied potential *versus* time during the forward scan of CV analysis at 10 mV/s to estimate the actual scan rate of the NiO$_x$H$_y$/FTO electrode employing different methods and degrees of *iR* compensation in **Figures 2a** and **3a**: (a,b) CI, (c) PF 100%, (d) No iR, and (e) Post 100%.

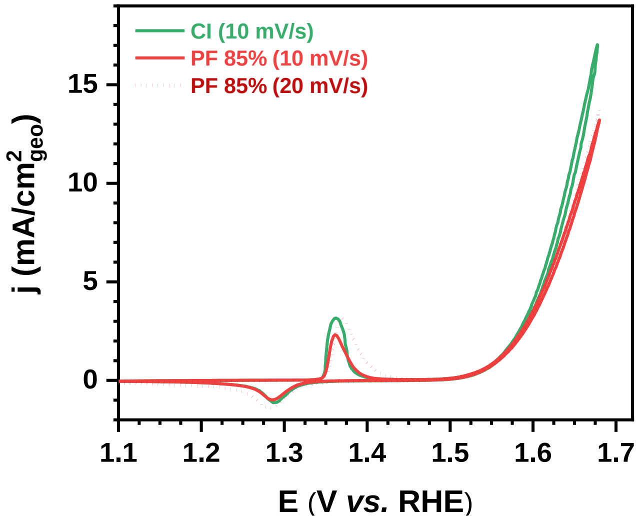

Figure S34. Comparison of j_{pa} of the NiO_xH_y/FTO electrode in **Figures 2a** and **3a** employing different *iR* compensation methods (*e.g.*, CI and PF) and scan rates (*i.e.*, 10 and 20 mV/s).

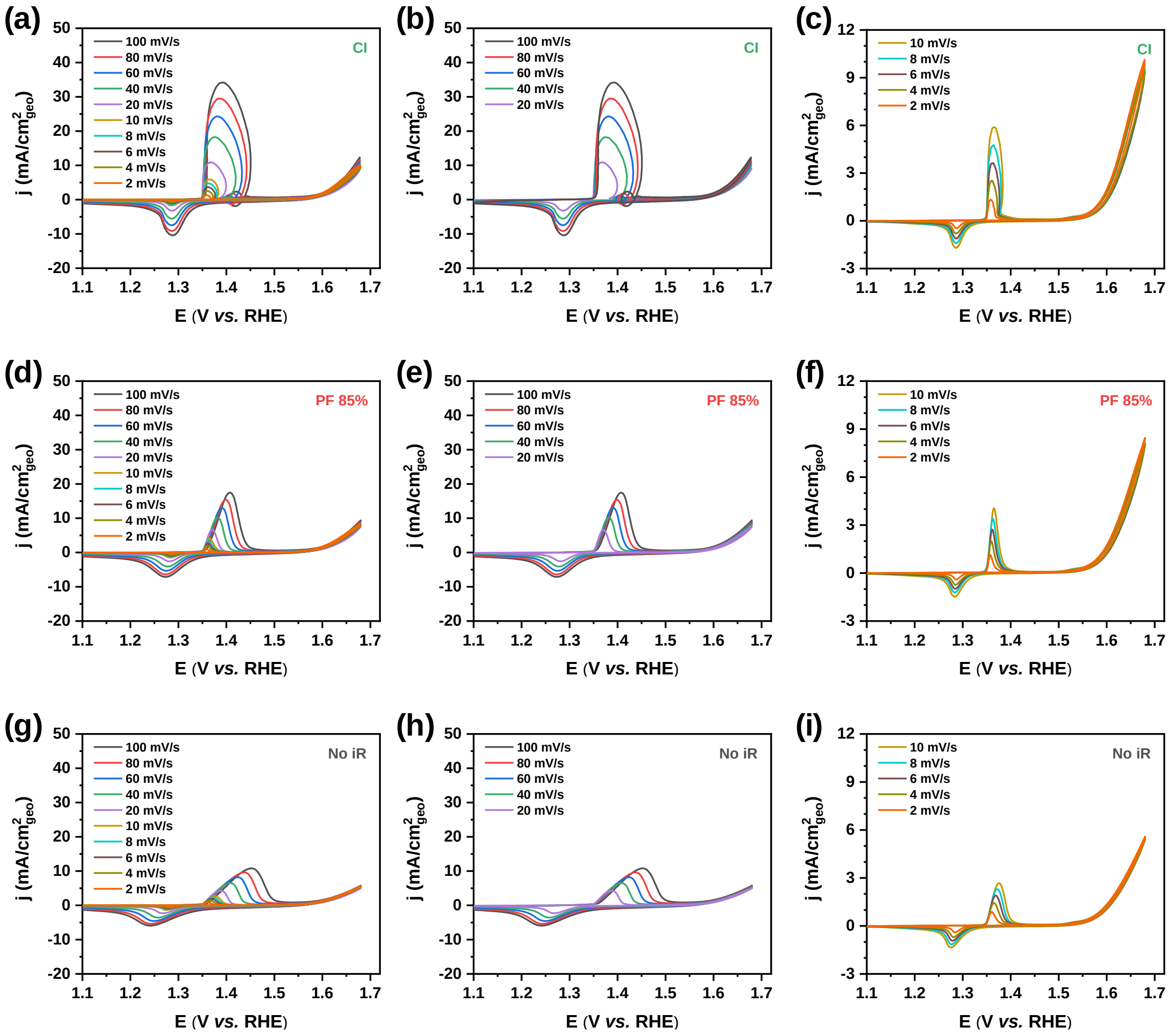

Figure S35. CV analyses of the Ni(OH)$_2$/FTO electrode employing different methods and degrees of *iR* compensation at various scan rates: (a-c) CI, (d-f) PF 85%, and (g-i) No iR.

Table S4. Variation of maximum actual scan rate with set scan rate for the NiO_xH_y/FTO electrode employing the CI compensation method in **Figure S35**.

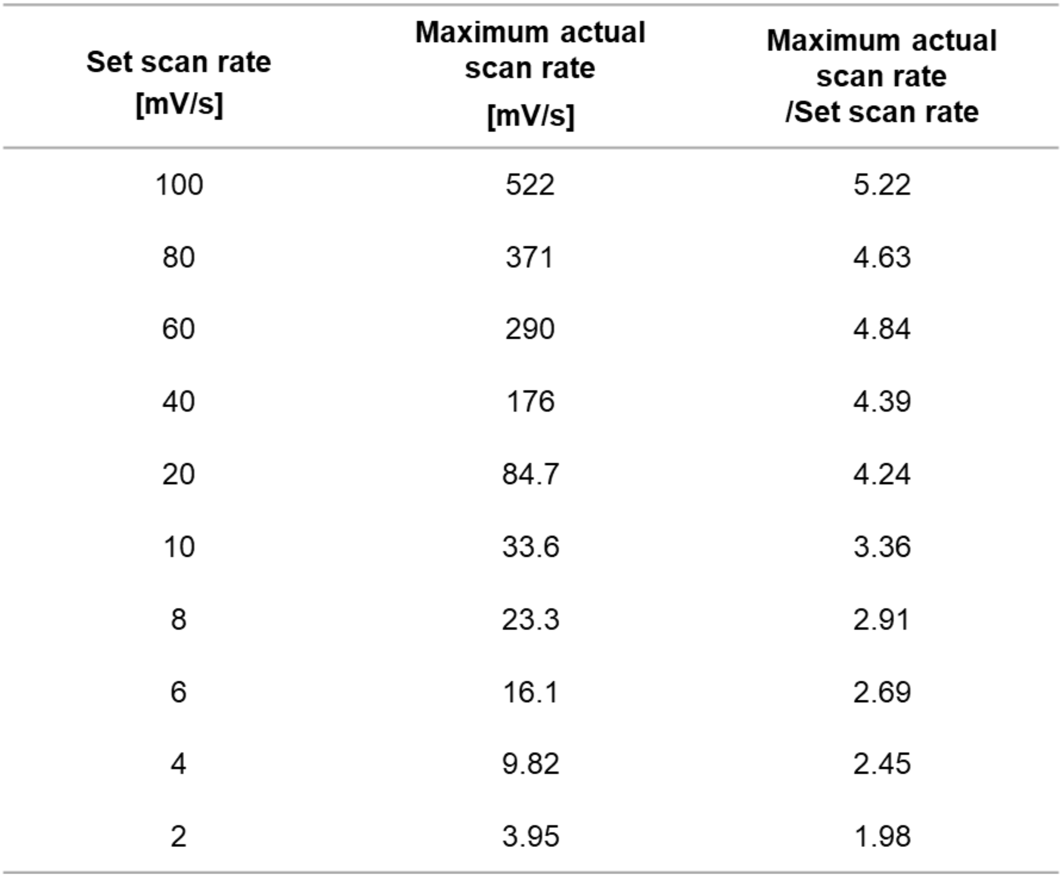

Set scan rate [mV/s]	Maximum actual scan rate [mV/s]	Maximum actual scan rate /Set scan rate
100	522	5.22
80	371	4.63
60	290	4.84
40	176	4.39
20	84.7	4.24
10	33.6	3.36
8	23.3	2.91
6	16.1	2.69
4	9.82	2.45
2	3.95	1.98

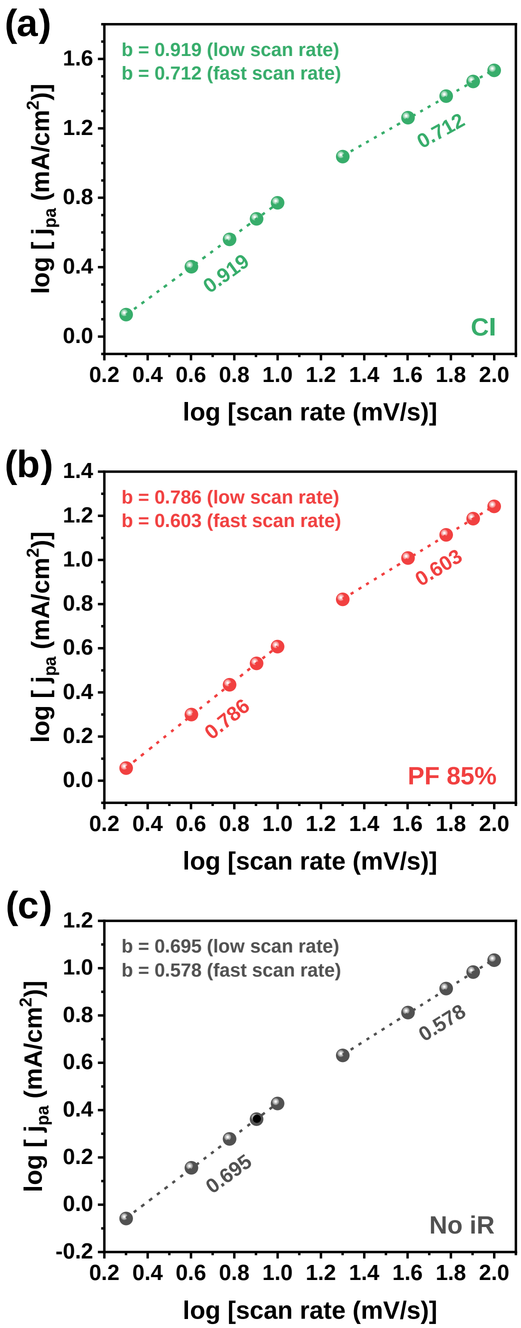

Figure S36. Linear plots of log [j_{pa}] *versus* log [scan rate] of the Ni(OH)$_2$/FTO electrode employing different methods and degrees of *iR* compensation in **Figure S35**: (a) CI, (b) PF 85%, and (c) No iR.

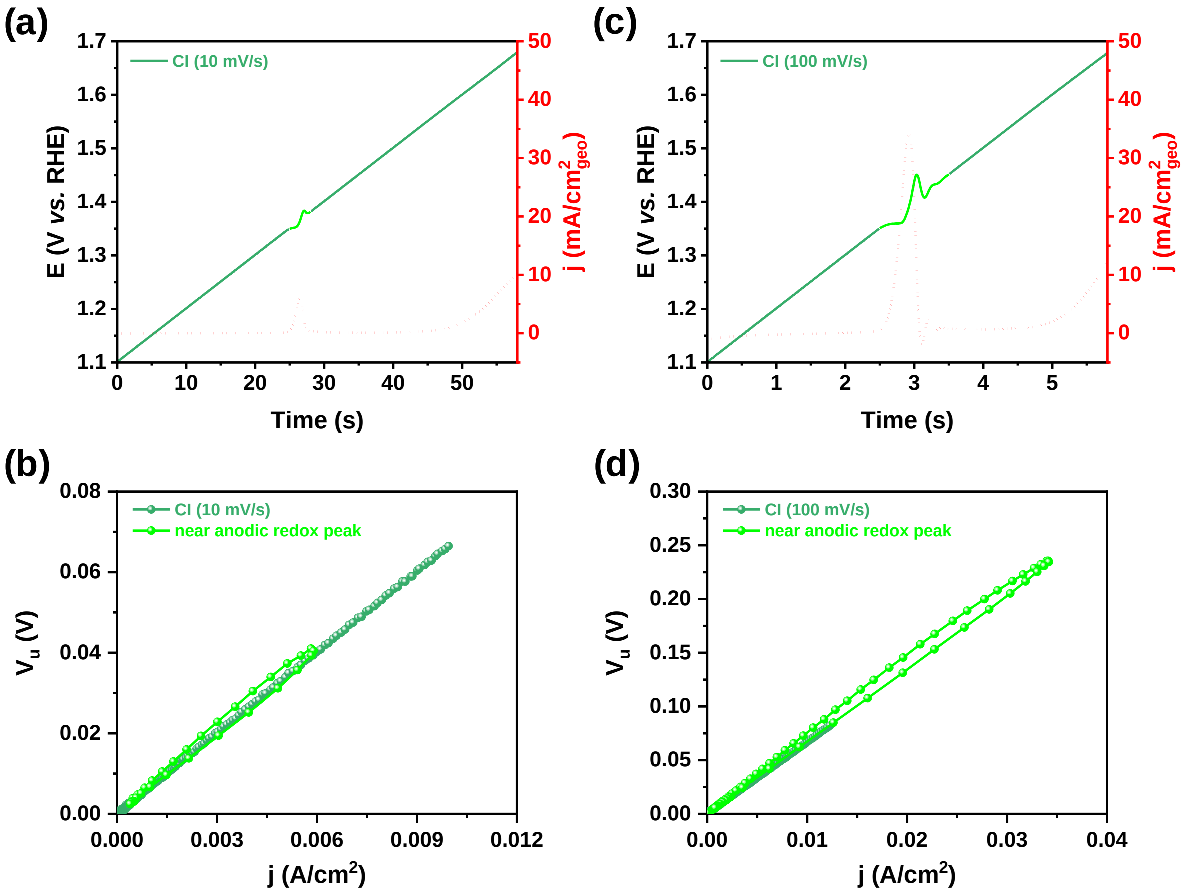

Figure S37. Plots of (a,c) applied potential *versus* time and (b,d) V_u *versus* j for the NiO$_x$H$_y$/FTO electrode employing CI in **Figure S35a-c** at a scan rate of (a,b) 10 mV/s and (c,d) 100 mV/s.

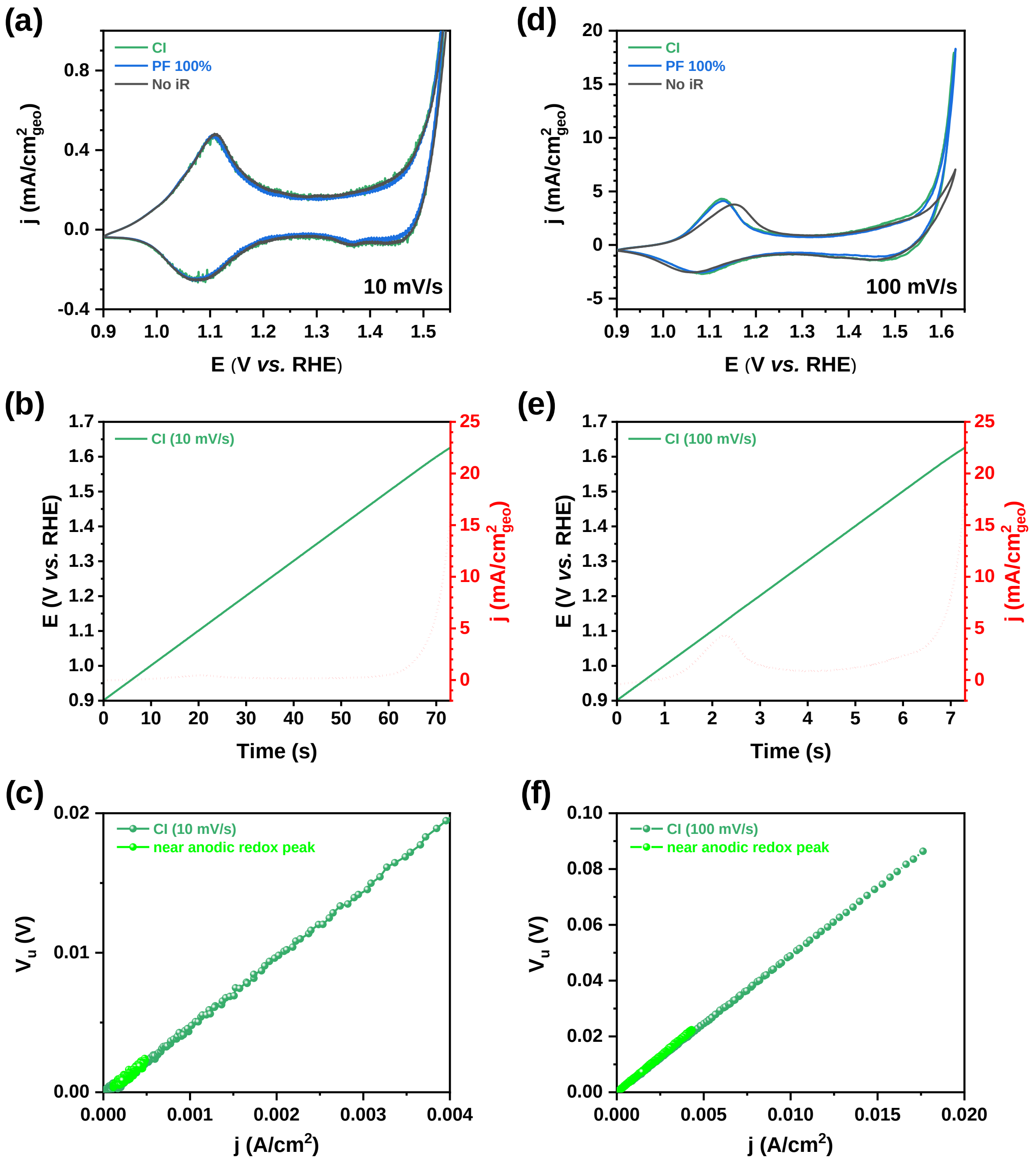

Figure S38. (a,d) CV curves and plots of (b,e) applied potential *versus* time and (c,f) V_u *versus* j of the CoO_xH_y/FTO electrode employing CI at a scan rate of (a-c) 10 mV/s and (d-f) 100 mV/s.

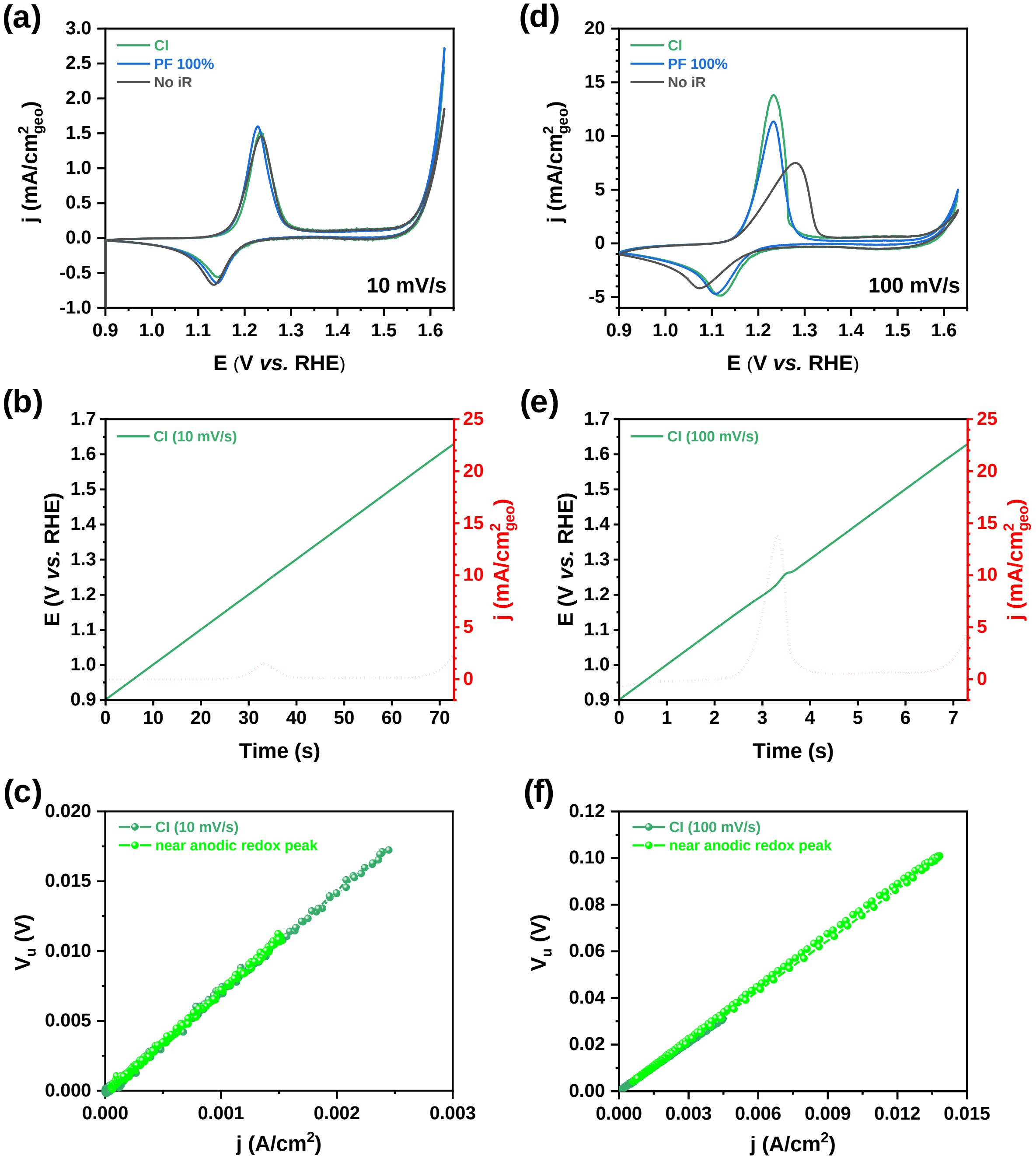

Figure S39. (a,d) CV curves and plots of (b,e) applied potential *versus* time and (c,f) V_u *versus* j of the NiCoO$_x$H$_y$/FTO electrode employing CI at a scan rate of (a-c) 10 mV/s and (d-f) 100 mV/s.

Supporting Note 4. Redox peak distortion

4.1. Impact of set scan rate and electrical conductivity

To investigate the underlying cause of the varying actual scan rate, control experiments were conducted by altering the set scan rates during CV analysis of the NiO_xH_y/FTO electrode. The severity of the actual scan rate variation when employing the CI method increased as the set scan rate was elevated, as demonstrated in **Figures S35**, **S37**, and **Table S4**. Moreover, at fast scan rates (*e.g.*, 20−100 mV/s), the significant variation in actual scan rate resulted in pronounced distortion of the redox peak, characterized by its backward bending, as shown in **Figure S35b**. Additionally, it was observed that the variation in actual scan rate can result in a different scan-rate dependency of the redox peak current density between the CI and PF method. Consequently, the *b*-value, which distinguishes the characteristics of the redox reaction as diffusion-controlled (b = 0.5) or surface-controlled (b = 1),[9] can exhibit higher values for the CI method compared to the PF method, as shown in **Figure S36**.

To further investigate the origin of actual scan rate variation for the CI method, other OER catalysts with different electrical conductivity than NiO_xH_y, such as CoO_xH_y, and $NiCoO_xH_y$, were examined.[7] CoO_xH_y/FTO and $NiCoO_xH_y$/FTO electrodes were prepared, and CV and actual scan rate analyses were performed at set scan rates of 10 and 100 mV/s. As shown in **Figure S37**, NiO_xH_y/FTO electrode exhibited actual scan rate variation at both set scan rates of 10 and 100 mV/s. In contrast, CoO_xH_y, which has superior electrical conductivity compared to NiO_xH_y, did not display actual scan rate variation at either 10 or 100 mV/s (**Figure S38**). Moreover, $NiCoO_xH_y$/FTO, which possesses moderate electrical conductivity between NiO_xH_y and CoO_xH_y, did not exhibit scan rate variation at 10 mV/s but showed actual scan rate variation at 100 mV/s. (**Figure S39**). These results indicate that the electrical conductivity of the catalyst layer can play a role in determining the presence of actual scan rate variation when employing the CI method.

4.2. Origin of actual scan rate variation for CI

We discovered that the degree of V_u fluctuation is consistent with the extent of actual scan rate variation. For instance, when the scan rate was set at 10 mV/s during the CV analysis, the NiO_xH_y/FTO electrode exhibited both actual scan rate variation and V_u fluctuation near the anodic redox peak (**Figure S37a,b**). When the extent of actual scan rate variation became more pronounced at 100 mV/s compared to 10 mV/s, more significant V_u fluctuation occurred. (**Figure S37 c,d**). For the CoO_xH_y/FTO electrode without any actual scan rate variation at both 10 and 100 mV/s, no V_u fluctuation was observed (**Figure S38**). In the case of the $NiCoO_xH_y$/FTO electrode, when there was no actual scan rate variation at 10 mV/s, V_u fluctuation was not observed. However, when a slight actual scan rate variation was present at 100 mV/s, a mild V_u fluctuation was observed (**Figure S39**). Furthermore, it is worth noting that since the extent of actual scan rate variation was less severe for $NiCoO_xH_y$/FTO compared to NiO_xH_y/FTO at 100 mV/s, the $NiCoO_xH_y$/FTO electrode exhibited a lower level of V_u fluctuation compared to the NiO_xH_y/FTO electrode.

Based on the aforementioned experimental findings, a substantial correlation has been established between V_u fluctuation and actual scan rate variation. Building upon this correlation and the principle of *iR* compensation (where the *iR*-compensated potential is equal to the applied potential plus the *iR* potential drop), it is presumed that V_u fluctuation induces variation in the actual scan rate by artificially altering the level of *iR* compensation. To be specific, when V_u fluctuation, which corresponds to R_u fluctuation, occurs, it causes an excessive or insufficient *iR* compensation compared to the correct level. As a consequence, the potential window scanned per unit time becomes larger or smaller than the correct potential window, resulting in variations in the actual scan rate near the redox peak.

The origin of V_u fluctuation near the redox peak can be attributed to a sudden change in the capacitance of the catalyst layer during the redox reaction of $M^{2+/3+}$. The condition for this phenomenon is that OER catalysts possess low electrical conductivity for $M(OH)_2$ phase (M^{2+}) and undergo a substantial change in electrical conductivity during the redox reaction of $M^{2+/3+}$. For instance, in the case of NiO_xH_y/FTO electrode, the electrical conductivity of $Ni(OH)_2$ is extremely low, rendering it almost insulating. When the electrode operates at potentials below the anodic redox potential of $Ni^{2+/3+}$ and NiO_xH_y catalyst layer remains as $Ni(OH)_2$ phase, the capacitance of $Ni(OH)_2$ catalyst layer cannot be measured due to its insulating nature. Instead, the capacitance of the conductive FTO substrate is measured as the capacitance of the NiO_xH_y /FTO electrode.[10] However, when the applied potential exceeds the anodic redox potential of $Ni^{2+/3+}$, a significant conductivity enhancement occurs within the NiO_xH_y catalyst layer due to the phase transformation of insulating $Ni(OH)_2$ to conductive NiOOH. Consequently, during the electrochemical analysis, the capacitance of the conductive NiOOH catalyst layer becomes evident and is reflected in the overall capacitance measured for NiO_xH_y/FTO electrode.[10] This leads to a significant *in situ* variation in the capacitance of the NiO_xH_y/FTO electrode during the redox reaction of $Ni^{2+/3+}$.[1,10] This variation is primarily due to the contrasting structural properties between the conductive substrate and MOOH catalyst layer. The conductive substrate shows the capacitance corresponding to its two-dimensional top surface area, while the MOOH catalyst layer, which typically possesses an electrolyte-permeable, hydrous structure, exhibits a considerably larger area at the catalyst/electrolyte interface in a three-dimensional space. Given the critical role of the faradaic capacitance during the current interruption, as explained in **Supporting Note 2.6**, any abrupt variation in capacitance can potentially disrupt the measurement of V_u during the current interruption process, resulting in V_u fluctuation.

To summarize, when OER catalysts exhibit low electrical conductivity in the $M(OH)_2$ phase and undergo significant conductivity enhancement during the redox reaction of $M^{2+/3+}$, it can lead to a sudden variation in capacitance. This capacitance variation can subsequently cause V_u fluctuation during the current interruption. As a consequence, the level of *iR* compensation is affected, resulting in changes to the potential window and actual scan rate during the potentiodynamic analysis. This summarized principle can provide an explanation for the increased severity of redox peak distortion and actual scan rate variation at higher scan rates. The higher scan rates expedite the phase transformation of $M(OH)_2$ to MOOH, leading to more rapid and abrupt changes in capacitance. As a result, the V_u fluctuation becomes amplified, intensifying the variation in the actual scan rate.

Moreover, this principle can elucidate the observed differences in actual scan rate variation near redox peak among OER catalysts with distinct electrical conductivity. For instance, in the case of the CoO_xH_y/FTO electrode, although CoO_xH_y catalyst undergoes conductivity enhancement during the anodic redox reaction of $Co^{2+/3+}$, the variation in capacitance before and after the redox reaction is not substantial. This is because the initial electrical conductivity of $Co(OH)_2$ is already sufficiently high, resulting in the capacitance of $Co(OH)_2$ catalyst layer being adequately reflected in the overall capacitance of the CoO_xH_y/FTO electrode.[2,11] Therefore, only a small increase in capacitance occurs after the anodic redox reaction, which is primarily caused by the higher electrical conductivity of CoOOH compared to $Co(OH)_2$. This minor variation in capacitance does not cause significant disruption in V_u measurement during the current interruption.

Consequently, no noticeable actual scan rate variation is observed for the CoO_xH_y/FTO electrode near its redox peak. On the other hand, in the case of the $NiCoO_xH_y$/FTO electrode, due to the moderate electrical conductivity of $NiCo(OH)_2$, which lies between the insulating $Ni(OH)_2$ and conductive $Co(OH)_2$,[7] the capacitance variation during the redox reaction of $M^{2+/3+}$ is expected to be intermediate between those of NiO_xH_y and CoO_xH_y. Hence, the V_u fluctuation and actual scan rate variation were only observable at a high scan rate of 100 mV/s, but not at 10 mV/s.

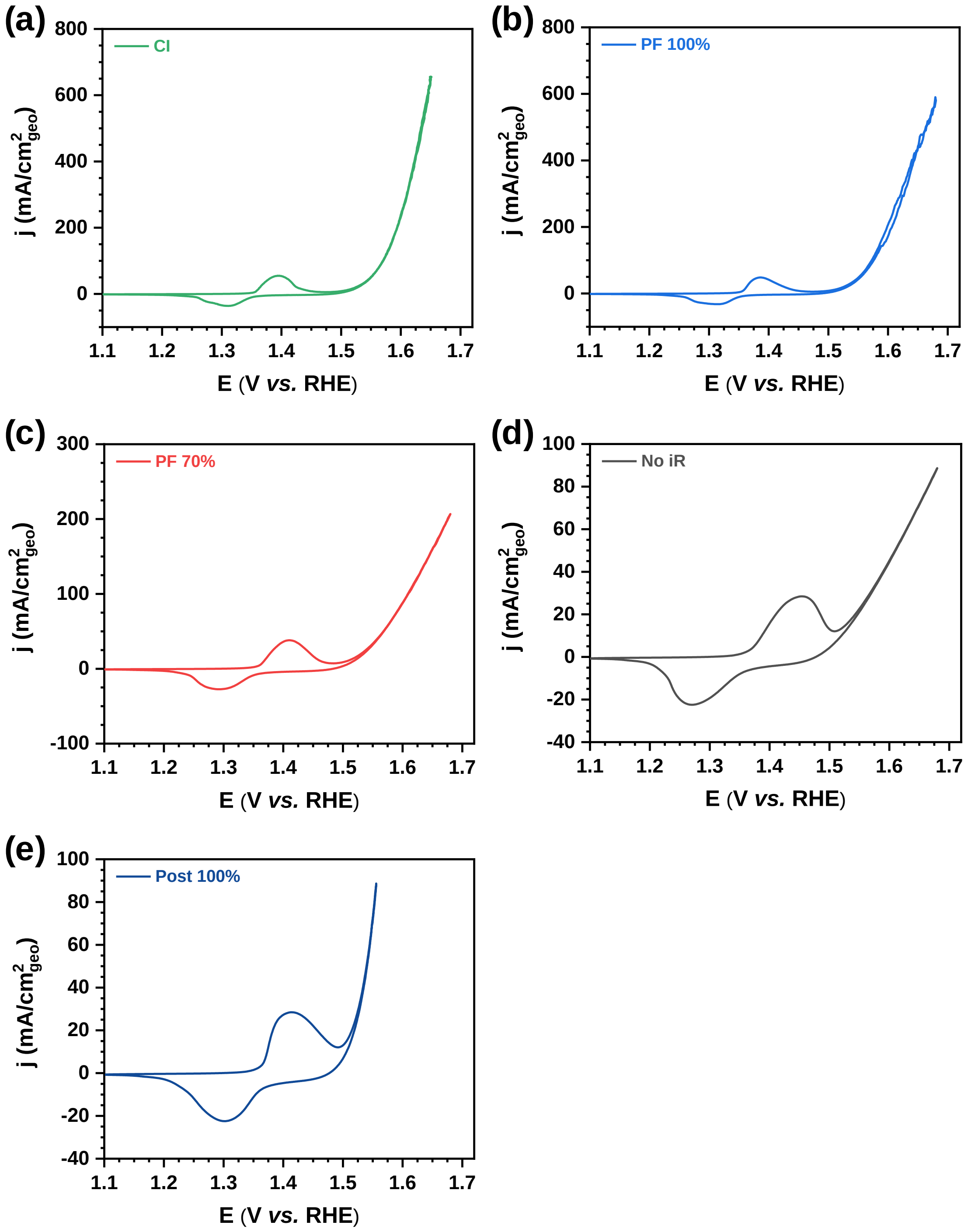

Figure S40. CV curves of the nanoporous NiO_xH_y/Ni foam electrode employing different methods and degrees of *iR* compensation in **Figures 2c**: (a) CI, (b) PF 100%, (c) PF 70%, (d) No iR, and (e) Post 100%.

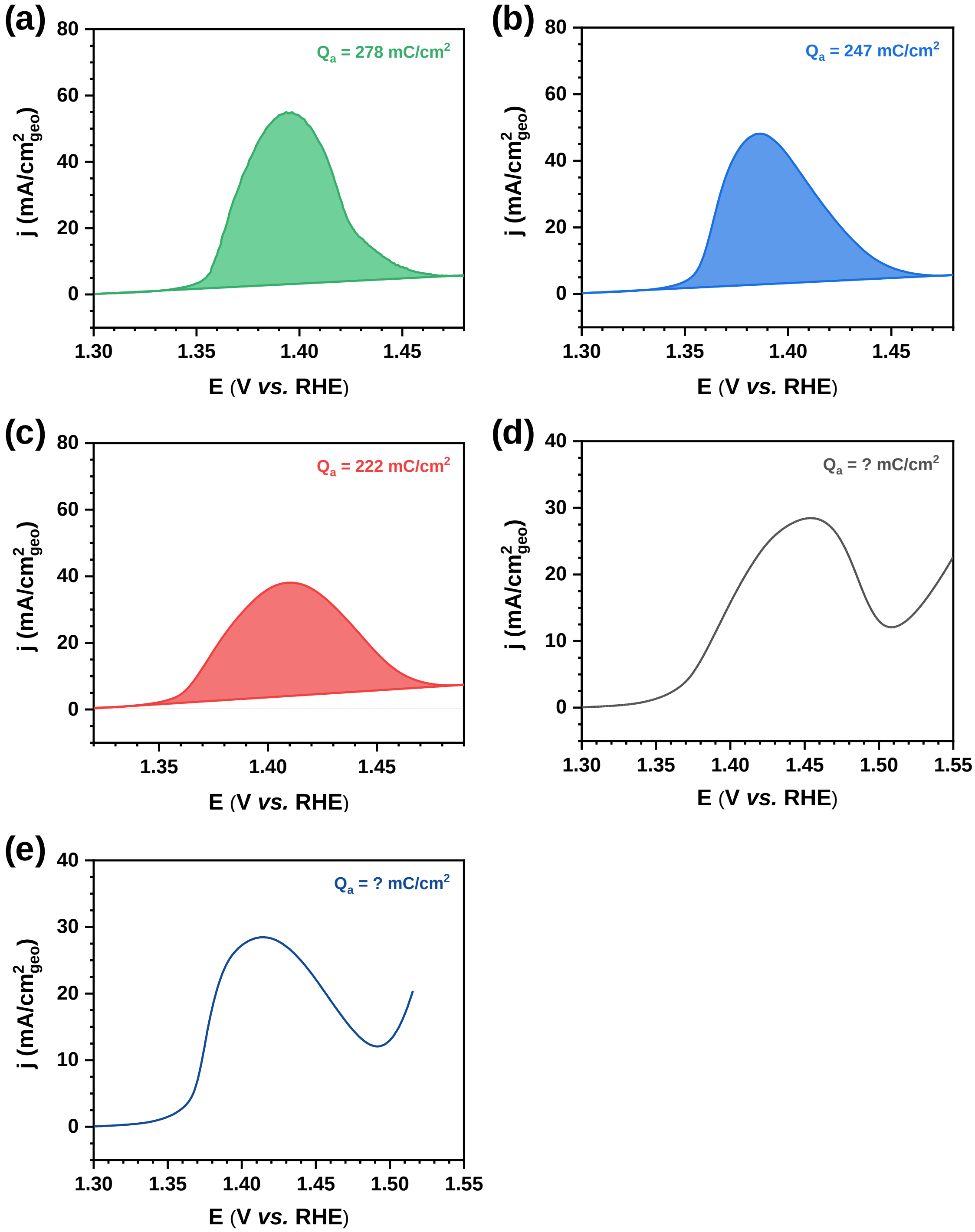

Figure S41. Estimation of Q_a of the nanoporous NiO_xH_y/Ni foam electrode employing different methods and degrees of *iR* compensation in **Figures 2c** and **3b**.

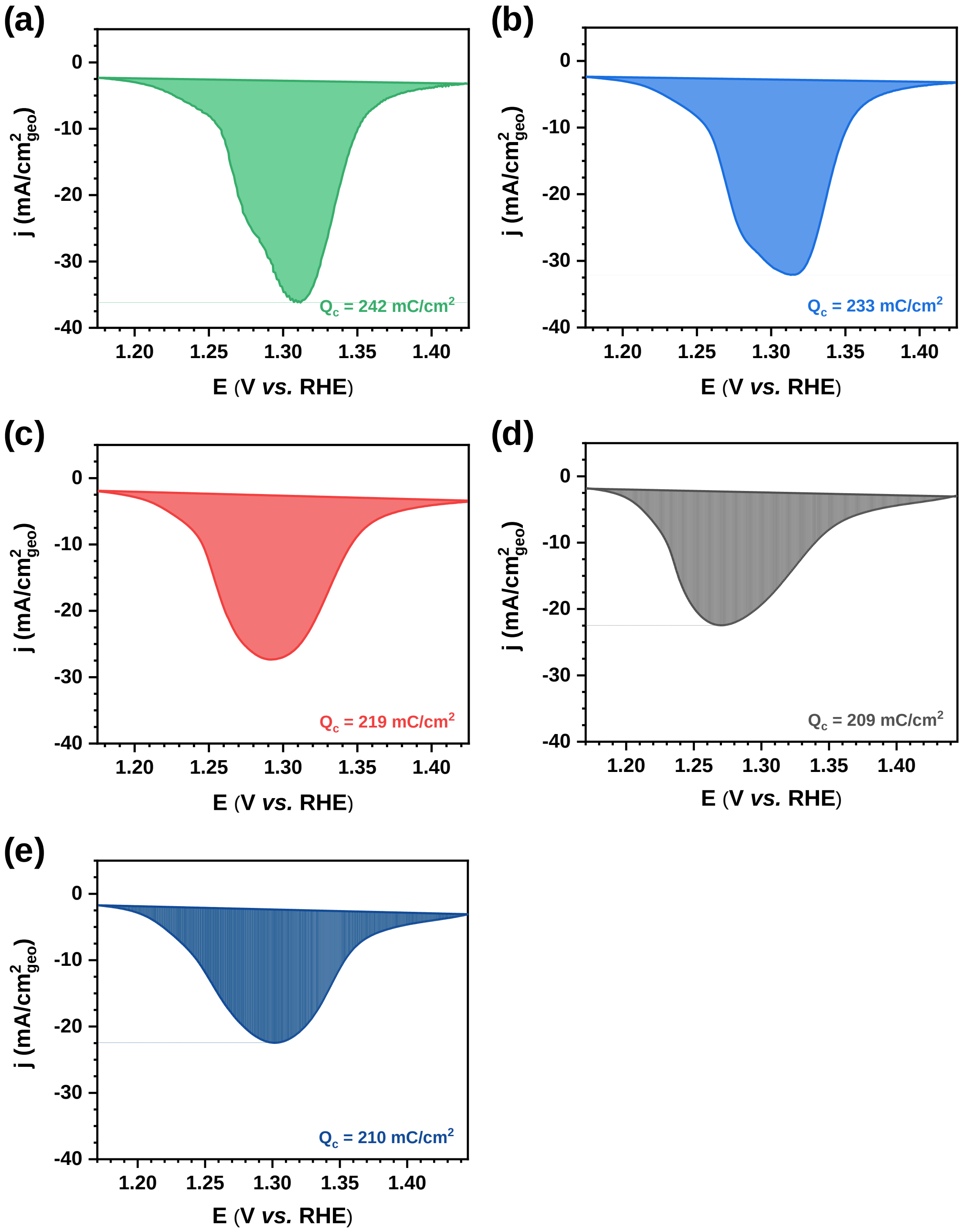

Figure S42. Estimation of Q_c of the nanoporous NiO_xH_y/Ni foam electrode employing different methods and degrees of *iR* compensation in **Figures 2c** and **3b**.

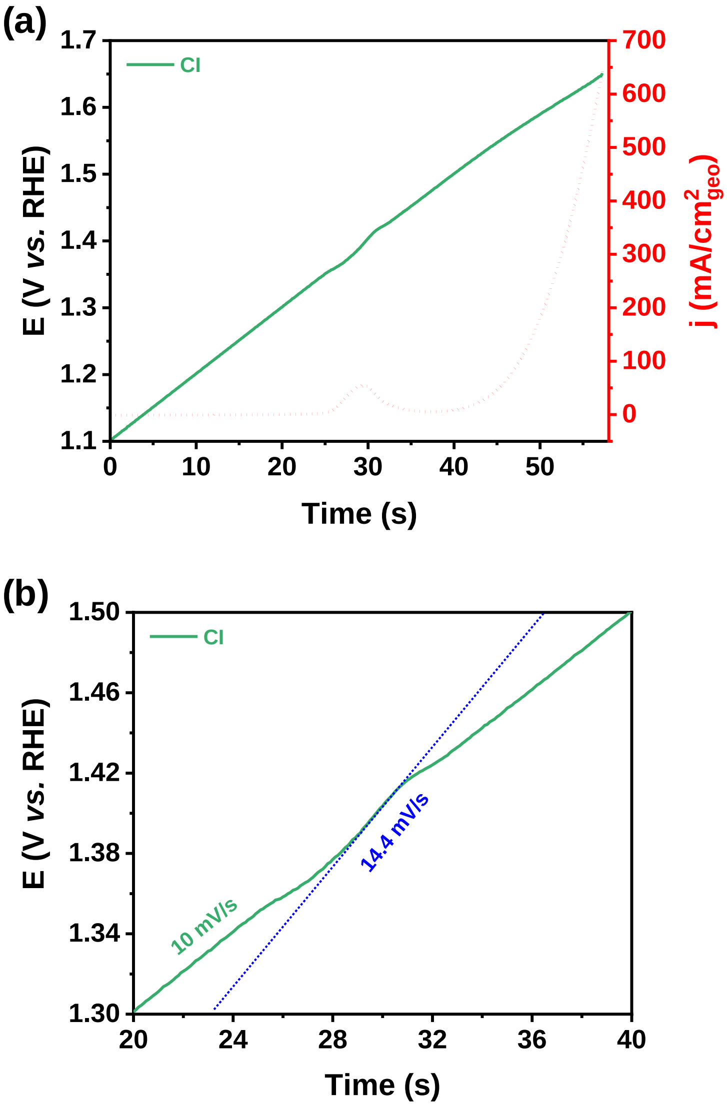

Figure S43. Plots of applied potential *versus* time during the forward scan of CV analysis to estimate the actual scan rate of the nanoporous NiO_xH_y/Ni foam electrode employing CI in **Figures 2c** and **3b**.

Supporting Note 5. Impact of characteristics of electrochemical system on R_u measurement

The characteristics of the electrode holder and substrate, including their resistance to surface oxidation and electrical conductivity, play a role in determining the presence and magnitude of the contact impedance. Additionally, the substrates with relatively poor electrical conductivity (*e.g.*, FTO substrate) compared to the metallic conductive substrates (*e.g.*, Ni foil and Ni foam) may have non-uniform R_{et} depending on the location due to the in-plane potential gradient on the substrate. This non-uniform R_{et} can change the R_u depending on the location, possibly influencing the shape of the redox peak. Furthermore, the experimental set-up and methodology of the electrochemical system, such as how the electrode is immersed in the electrolyte and how the magnetic bar is stirred in an electrochemical cell, can affect the growth of contact impedance on the electrode holder and substrate during the electrochemical testing. Regarding the properties of the catalyst layer, both material properties (*e.g.*, initial electrical conductivity of $M(OH)_2$ and the extent of conductivity enhancement during the M^{2+}/M^{3+} redox reaction) and structural properties (*e.g.*, compact or porous morphology, thickness, and composite structure) determine the presence and significance of R_{et} in the measured R_u, as well as the presence and significance of actual scan rate variation near the redox peak for the CI method. Moreover, the electrochemical (EC) testing conditions, such as the applied potential and operating current density, can impact the presence and significance of R_{et} and R_{bubble} in the measured R_u. Additionally, other experimental variables related to the electrolyte, such as the change in temperature and ionic conductivity of the electrolyte during the long-term stability test or the flow rate of the electrolyte within the flow cell system, can affect the solution resistance in the measured R_u.

Supporting Note 6. Recommendations and cautions about appropriate R_u, degree of *iR* compensation, and *iR* compensation method

Regarding the appropriate R_u for *iR* compensation, it is generally recommended to use either $R_{u,EIS,1}$ (above anodic redox potential) or $R_{u,EIS,2}$ (in cases where contact impedance arises from the electrode connector/substrate interface). This choice ensures that the performance of the catalytic electrode can be fairly compared with results reported in other studies. However, it is worth noting that different R_u values, each with different physical meanings, can be employed for *iR* compensation depending on the specific purpose and focus of the study (*e.g.*, intrinsic activity, sample activity, electrode activity, *etc.*). Below, we provide a summary of the physical meaning of R_u values for an OER catalytic electrode consisting of a dense NiO_xH_y catalyst layer on the substrate.

(i) In the absence of contact impedance

$R_{u,EIS}$ (below anodic redox potential) = R_{sol} + R_{et} (catalytically non-active phase + substrate)

$R_{u,EIS}$ (above anodic redox potential) = R_{sol} + R_{et} (catalytically active phase + substrate)

$R_{u,CI}$ = R_{sol} + R_{et} (catalytically active phase + substrate) + (R_{bubble} , if significant)

(ii) In the presence of contact impedance

$R_{u,EIS,1}$ (below anodic redox potential) = R_{sol} + R_{et} (catalytically non-active phase + substrate)

$R_{u,EIS,1}$ (above anodic redox potential) = R_{sol} + R_{et} (catalytically active phase + substrate)

$R_{u,EIS,2}$ (above anodic redox potential) = R_{sol} + R_{et} (catalytically active phase + substrate) + $R_{contact}$

$R_{u,CI}$ (contact impedance with sufficiently small RC time constant) = Incorrect

$R_{u,CI}$ (contact impedance with sufficiently high RC time constant) = R_{sol} + R_{et} (catalytically active phase + substrate) + ($R_{bubble,}$ if significant)

Regarding the degree of *iR* compensation, it is advisable to use 100% compensation when assessing catalytic performance, regardless of the specific *iR* compensation method employed. In addition, employing 100% compensation offers greater accuracy in analyzing the redox peak, as it allows for precise measurement of peak shape and current. This approach also mitigates the risk of obtaining different redox charges, especially in the case of oxide-based OER electrodes prone to charge trapping issues.

There are several cautions when using different *iR* compensation methods. While Post 100% compensation is suitable for evaluating catalytic performance, it may not be the best choice for analyzing the redox peak properties, such as its shape and sensitivity to scan rate. On the other hand, PF 100% compensation is optimal for both assessing electrocatalytic performance and examining the redox peak. However, if PF 100% compensation causes oscillations due to errors or overcompensation, possibly stemming from inaccuracies in R_u values,[5] or phase shifts introduced by cell components and amplifiers,[12] an alternative approach is to combine PF and post-*iR* compensation. This combined method can be employed to evaluate catalytic performance effectively. Note that, in our experience, minimizing and preventing oscillations when using a high degree of *iR* compensation (*e.g.*, 98% or 100%) with PF can be achieved by using accurate R_u value, maintaining low current levels, and utilizing cell components that introduce minimal phase shift.

CI can also be utilized to investigate both catalytic performance and the redox peak, provided that specific conditions are met. These conditions include the absence of two key factors: (1) contact impedance characterized by a sufficiently small RC time constant and (2) significant variations in capacitance during the redox reaction of the electrode. When the operating current does not induce pronounced bubble generation and accumulation, CI can be applied similarly to PF 100% and Post 100% compensation. Furthermore, for those interested in studying the impact of bubble resistance on OER performance at high OER currents, CI can be employed and compared with PF 100% or Post 100% compensation. Nevertheless, given the complexities and necessary precautions when using CI, the typical and recommended approach is to favor PF 100% or Post 100% compensation utilizing $R_{u,EIS}$ measured at faradic potentials.

REFERENCES

(1) Son, Y. J.; Kawashima, K.; Wygant, B. R.; Lam, C. H.; Burrow, J. N.; Celio, H.; Dolocan, A.; Ekerdt, J. G.; Mullins, C. B. Anodized Nickel Foam for Oxygen Evolution Reaction in Fe-Free and Unpurified Alkaline Electrolytes at High Current Densities. *ACS Nano* **2021**, *15* (2), 3468–3480.

(2) Trotochaud, L.; Young, S. L.; Ranney, J. K.; Boettcher, S. W. Nickel–Iron Oxyhydroxide Oxygen-Evolution Electrocatalysts: The Role of Intentional and Incidental Iron Incorporation. *J. Am. Chem. Soc.* **2014**, *136* (18), 6744–6753.

(3) Márquez, R. A.; Kawashima, K.; Son, Y. J.; Castelino, G.; Miller, N.; Smith, L. A.; Chukwuneke, C. E.; Mullins, C. B. Getting the Basics Right: Preparing Alkaline Electrolytes for Electrochemical Applications. *ACS Energy Lett.* **2023**, *8* (2), 1141–1146.

(4) Zheng, W.; Liu, M.; Lee, L. Y. S. Best Practices in Using Foam-Type Electrodes for Electrocatalytic Performance Benchmark. *ACS Energy Lett.* **2020**, *5* (10), 3260–3264.

(5) Zheng, W. IR Compensation for Electrocatalysis Studies: Considerations and Recommendations. *ACS Energy Lett.* **2023**, *8* (4), 1952–1958.

(6) Gamry Instruments. Application Note: Understanding iR Compensation. https://www.gamry.com/application-notes/instrumentation/understanding-ir-compensation/

(7) Stevens, M. B.; Enman, L. J.; Batchellor, A. S.; Cosby, M. R.; Vise, A. E.; Trang, C. D. M.; Boettcher, S. W. Measurement Techniques for the Study of Thin Film Heterogeneous Water Oxidation Electrocatalysts. *Chem. Mater.* **2017**, *29* (1), 120–140.

(8) Chung, D. Y.; Park, S.; Lopes, P. P.; Stamenkovic, V. R.; Sung, Y.-E.; Markovic, N. M.; Strmcnik, D. Electrokinetic Analysis of Poorly Conductive Electrocatalytic Materials. *ACS Catal.* **2020**, *10* (9), 4990–4996.

(9) Son, Y. J.; Kim, S.; Leung, V.; Kawashima, K.; Noh, J.; Kim, K.; Marquez, R. A.; Carrasco-Jaim, O. A.; Smith, L. A.; Celio, H.; Milliron, D. J.; Korgel, B. A.; Mullins, C. B. Effects of Electrochemical Conditioning on Nickel-Based Oxygen Evolution Electrocatalysts. *ACS Catal.* **2022**, *12* (16), 10384–10399.

(10) Batchellor, A. S.; Boettcher, S. W. Pulse-Electrodeposited Ni–Fe (Oxy)Hydroxide Oxygen Evolution Electrocatalysts with High Geometric and Intrinsic Activities at Large Mass Loadings. *ACS Catal.* **2015**, *5* (11), 6680–6689.

(11) Mefford, J. T.; Akbashev, A. R.; Zhang, L.; Chueh, W. C. Electrochemical Reactivity of Faceted β-Co(OH)2 Single Crystal Platelet Particles in Alkaline Electrolytes. *J. Phys. Chem. C* **2019**, *123* (31), 18783–18794.

(12) Bard, A. J.; Faulkner, L. R. *Electrochemical Methods: Fundamentals and Applications*, 2nd ed.; John Wiley & Sons, Inc., New York, 2001.